JGR Atmospheres

RESEARCH ARTICLE
10.1029/2024JD042634

Key Points:
- Equatorial contribution to the global electric circuit (GEC) has two maxima following the equinoxes, nonequatorial contributions have one maximum in local summer
- The resulting annual variation of the GEC, being the sum of three clear patterns offsetting each other, is subtle and hard to simulate
- Simulations approach observations if contributions to the GEC are parameterized using surface air temperature besides convection parameters

Supporting Information:
Supporting Information may be found in the online version of this article.

Correspondence to:
N. N. Slyunyaev,
slyunyaev.n@ipfran.ru

Citation:
Slyunyaev, N. N., Sarafanov, F. G., Ilin, N. V., Mareev, E. A., Volodin, E. M., Frank-Kamenetsky, A. V., & Williams, E. R. (2025). The seasonal variation of the direct current global electric circuit: 2. Further analysis based on simulations. *Journal of Geophysical Research: Atmospheres*, *130*, e2024JD042634. https://doi.org/10.1029/2024JD042634

Received 3 OCT 2024
Accepted 31 MAR 2025

The Seasonal Variation of the Direct Current Global Electric Circuit: 2. Further Analysis Based on Simulations

Nikolay N. Slyunyaev[1], Fedor G. Sarafanov[1], Nikolay V. Ilin[1], Evgeny A. Mareev[1], Evgeny M. Volodin[2], Alexander V. Frank-Kamenetsky[3], and Earle R. Williams[4]

[1]Institute of Applied Physics, Russian Academy of Sciences, Nizhny Novgorod, Russia, [2]Institute of Numerical Mathematics, Russian Academy of Sciences, Moscow, Russia, [3]Arctic and Antarctic Research Institute, St. Petersburg, Russia, [4]Parsons Laboratory of the Department of Civil and Environmental Engineering, Massachusetts Institute of Technology, Cambridge, MA, USA

Abstract Both simulations and measurements indicate the existence of stable annual behavior of the global electric circuit (GEC) intensity, but the exact pattern of variation is very difficult to reliably determine. Here we present further analysis of this problem using the results of ionospheric potential (IP) simulations with two different models of atmospheric dynamics. From a theoretical perspective, the annual variation of the GEC is eventually determined by seasonal changes in the distribution of convection, associated with the annual cycle of insolation. Simulations clearly demonstrate that the contribution to the IP from the vicinity of the equator has two maxima following the equinoxes, whereas the contribution of nonequatorial latitudes in each hemisphere has one maximum during the local summer. The resulting seasonal variation of the GEC, being the sum of three clear patterns offsetting each other, is rather subtle, and its prediction in simulations may vary depending on the model and IP parameterization. It is likely that the actual seasonal variation of the diurnal mean GEC intensity has one pronounced maximum during the Northern Hemisphere summer and one pronounced minimum during the Northern Hemisphere winter, in agreement with potential gradient measurements in Antarctica and in agreement with the larger portion of the Northern Hemisphere occupied by land. Physical parameters characterizing convection do not provide a very good measure of contributions to the IP, notably overestimating the role of equatorial latitudes; by including surface air temperature in the IP parameterization, one can achieve a better agreement between simulations and observations.

Plain Language Summary The global electric circuit (GEC) is an overarching concept in atmospheric electricity, according to which electrified clouds generate a distribution of electromagnetic fields all over the Earth. Notwithstanding that the annual cycle of summer and winter is the largest cause of atmospheric variations on Earth, the seasonal variation of the GEC is still not reliably known, since measurements of atmospheric electrical parameters do not yield a comprehensive answer. In Part 1 of this study we investigated this problem using the results of electric field measurements in Antarctica, and here we further analyze the question using the results of ionospheric potential simulations with models of atmospheric dynamics. The annual behavior of the GEC is eventually determined by seasonal changes in global convection patterns, associated with the annual cycle of insolation and influenced by the distribution of land over the Earth's surface. We explain why the resulting pattern of variation is rather subtle and difficult to reliably determine from simulations and measurements. In Part 1 of this study we concluded that the actual GEC intensity is likely to be at a maximum during the Northern Hemisphere summer, and now simulations give us a more detailed physical explanation for such behavior.

1. Introduction

The idea of the direct current (DC) global electric circuit (GEC) was originally proposed by Wilson (1921). It suggests that electrified clouds in the atmosphere (including thunderstorms) serve as current generators maintaining a distribution of quasi-stationary electromagnetic fields and currents all over the Earth's surface (see, e.g., Rycroft et al., 2008; Williams, 2009; Williams & Mareev, 2014). More precisely, in the regions occupied by electrified clouds charge separation inside them produces an upward flow of the electric current, which is compensated by a downward flow in fair-weather regions, the Earth's surface and ionosphere completing the circuit. By analogy with the DC GEC, global electromagnetic resonances excited in the Earth—ionosphere cavity by lightning are often called the alternating current (AC) GEC; the AC GEC will not be considered in this study, and from now on by GEC we shall always mean the DC GEC.

Thus, the GEC links the regions occupied by electrified clouds to fair-weather regions. This implies that measuring the potential gradient (PG) in fair-weather regions should allow one to infer some information about the dynamics of the global distribution of electrified clouds. In practice, however, surface PG values are usually substantially influenced by local conductivity perturbations due to radon and aerosols. In this connection PG measurements in clean locations (where the influence of these factors is absent or very small) are of special significance. Among such measurements, we can mention here atmospheric electrical observations on board the Carnegie ship in the Pacific, Atlantic, and Indian Oceans during 1915–1921 and 1928–1929 (Ault & Mauchly, 1926; Torreson et al., 1946) and on board the Maud ship in the Arctic Ocean during 1922–1925 (Sverdrup, 1926), as well as PG measurements at the Antarctic Plateau (e.g., Burns et al., 2012, 2017).

In addition to the fair-weather PG, it is also possible (albeit rather difficult) to measure the fair-weather air—Earth current density, which characterizes the GEC as well and is less affected by local perturbations. From a theoretical viewpoint, however, the most natural and fundamental characteristic of the GEC intensity is the so-called ionospheric potential (IP). It is defined as the potential of the lower ionosphere relative to the Earth's surface, which, according to the concept of the GEC, should always be more or less the same at different locations over the globe (as both atmospheric boundaries are supposed to be highly conductive and, by inference, nearly equipotential).

To actually measure the IP, one needs to integrate the vertical profile of the PG up to at least several kilometers above sea level (Markson, 2007), which requires aircraft or balloon soundings to determine this profile. Such measurements, when performed simultaneously at remote locations, indeed yield relatively close IP values (Markson et al., 1999; Mühleisen, 1971) and thus support the validity of the concept of the GEC. However, in general the existing IP data are scarce compared to the available results of surface PG and air—Earth current measurements, which is understandable in view of the fact that aircraft and balloon soundings are difficult and rather expensive. At the same time in theoretical discussions of atmospheric electricity the IP is the most natural and convenient measure of the GEC intensity: Using the superposition principle, one can naturally regard it as a sum of contributions from specific regions of the Earth's surface, which, in their turn, can be analyzed in connection with local weather and climate.

Measurements on board the Carnegie and Maud research vessels in 1915–1929 revealed the existence of a universal dependence of the mean fair-weather PG on the UTC hour, which looks almost the same even at remote locations (Mauchly, 1921, 1923; Sverdrup, 1926). This dependence is now known as the classical Carnegie curve; a somewhat similar diurnal curve was obtained before the Carnegie and Maud campaigns by Simpson (1906) on the basis of PG measurements in Karasjok, Lapland, but its significance was not understood at the time. Later the observed correlation between the Carnegie curve and the diurnal cycle of global thunderstorm activity (Whipple, 1929; Whipple & Scrase, 1936) has become an important piece of experimental evidence supporting the idea of the GEC; note, however, that besides thunderstorms, electrified shower clouds (i.e., electrified clouds without lightning) are equally important for maintaining the GEC, as noted already by Wilson (1921). Numerous later studies based on PG measurements in other locations (e.g., Burns et al., 2012; Harrison, 2003) and IP soundings (Markson, 1986; Mühleisen, 1977) yielded diurnal variations of the GEC similar to the classical Carnegie curve, although, strictly speaking, the latter does not represent the real average diurnal cycle owing to the nonuniform seasonal sampling of the Carnegie data (see Burns et al., 2017).

In the following years the Carnegie curve has been replicated using satellite data on precipitation (Liu et al., 2010) and the results of aircraft measurements of the so-called Wilson current, which flows over electrified clouds, together with global lightning statistics derived from satellite observations (Mach et al., 2011) or ground-based lightning location networks (Hutchins et al., 2014; Mezuman et al., 2014). What is more important, over the past decade the shape of the Carnegie curve has been successfully reproduced in simulations with several different climate and weather forecasting models (Ilin et al., 2020; Jánský et al., 2017; Lucas et al., 2015; Mareev & Volodin, 2014). In such studies charge separating currents inside electrified clouds are parameterized in terms of convection (whose parameters are determined in simulations), and then these currents are used to compute contributions to the IP. Even though large-scale simulations tend to underestimate the peak-to-peak amplitude of the diurnal variation of the GEC intensity, their ability to correctly predict the shape of this variation illustrates an important property of the GEC, which to a large extent determines the interest in its investigation: The variation of the GEC intensity reflects changes in global weather and climate through changes in global convection.

In addition to the diurnal cycle in the variation of GEC parameters, recent studies have revealed clear patterns related to tropical modes of atmospheric variability, namely to the El Niño—Southern Oscillation (Harrison et al., 2022; Lavigne et al., 2017; Slyunyaev, Frank-Kamenetsky, et al., 2021; Slyunyaev, Ilin, et al., 2021) and the Madden–Julian oscillation (Kozlov et al., 2023; Tacza et al., 2022). It is remarkable that these patterns have been identified not only in the results of fair-weather PG measurements but also in IP time series simulated with models of atmospheric dynamics, which has provided important insights into physical mechanisms behind the observed relationships and dependencies (Kozlov et al., 2023; Slyunyaev, Frank-Kamenetsky, et al., 2021).

It is natural to expect that the GEC variation also reflects the seasonal cycle of summers and winters, which can be thought of as the most pronounced mode of atmospheric variability. Just as the classical Carnegie curve (or its modern more accurate counterparts based on more recent data) represents the average diurnal behavior of the main GEC parameters, there should exist an analogous curve on the annual timescale. However, the numerous existing data sets of atmospheric electrical parameters demonstrate very different annual variations (often contradicting one another), and the real seasonal variation of the GEC is still not known and hard to determine.

First of all, fair-weather PG measurements over continents are known to yield seasonal variation curves dominated by annual cycles of local factors. Early atmospheric electricity observations had demonstrated that in the Northern Hemisphere the fair-weather PG is highest during the local winter (this was first noted by Lord Kelvin; see Thomson, 1860, later reprinted in Thomson (1884)), but it later turned out that in the Southern Hemisphere the PG behaves oppositely, reaching maximum values during the Northern Hemisphere summer (e.g., Halliday, 1933). A comprehensive analysis of this reversal in the pattern of variation between the two hemispheres was carried out by Adlerman and Williams (1996), who linked this phenomenon to much higher aerosol concentrations over continents during local winters, leading to smaller conductivity values and, by inference, to greater PG values.

This observation already implies that only PG variations obtained in clean locations can be representative of the actual global seasonal pattern; therefore, the aforementioned PG measurements over the ocean and in the Antarctic are of particular interest in the seasonal context too. Apart from that, there have been several attempts to infer the seasonal behavior of the GEC from the air—Earth current density data or IP data, which, in theory, should not be affected by local conductivity perturbations at the site where the observations were performed. In Part 1 of this study (published as a separate article, see Slyunyaev et al., 2025b), devoted to the discussion of the seasonal variation of the GEC from the perspective of observations, we tried to systematize and analyze the results known from the literature and further investigate the problem using the results of PG measurements at the Vostok station in Antarctica during 2006–2020.

First, we have pointed out that diurnal mean values of atmospheric electrical parameters and their values at specific UTC hours may manifest different seasonal behavior in view of the prominent seasonal change in the shape of the diurnal variation of the GEC (e.g., Burns et al., 2017). This means that we should not consider the results based on air—Earth current density measurements at specific hours (e.g., Harrison & Ingram, 2005; Harrison & Nicoll, 2008) if we want to discuss seasonal changes in the diurnal mean GEC intensity. The same can be said about IP measurements (summarized by Markson (2007)), as the available data do not form a consistent time series, being obtained at irregular intervals and at different UTC hours, often by means of different instrumentation and at different locations, not to speak of nonuniform seasonal sampling.

Moreover, this argument also applies to the results of oceanic measurements during the Carnegie cruises. Despite their high quality, the Carnegie data do not form a consistent time series (complete 24-hr PG records are available only for a small number of fine days), which means that seasonal patterns inferred from these results may crucially depend on data selection criteria and averaging procedures. This expectation is supported by modern attempts to analyze the Carnegie data set: according to Adlerman and Williams (1996), the Carnegie PG values, together with the values recorded on board the Maud ship, reveal a summertime PG maximum, whereas Harrison and Nicoll (2008) found wintertime PG values in the Carnegie data to be generally higher.

Second, we have shown that the highest and lowest fair-weather PG values at Vostok occur during the Northern Hemisphere summer and winter, respectively. Such results follow from our analysis on the basis of the 2006–2020 Vostok time series, and they also generally agree with the results obtained at the same location earlier (in 1998–2001; see Burns et al., 2012). Adjusting Vostok PG values for local meteorological and solar wind influences reduces the peak-to-peak amplitude of the variation but does not change its overall appearance. Available results of continuous air—Earth current measurements (with complete 24-hr records) generally agree with the behavior of the PG at Vostok, indicating larger fair-weather current density values during the Northern Hemisphere summer and smaller values during the winter (see Adlerman & Williams, 1996; Retalis, 1991; Scrase, 1933). At the same time the peak-to-peak amplitudes of these current-based variation curves differ substantially, and each of them has its own local peculiarities.

Finally, we have shown that the PG variation observed at Vostok admits a clear physical interpretation. According to the remarks made above, the variation of the GEC on any timescale can be decomposed as the sum of variations of regional contributions to the IP, which, in their turn, reflect changes in the geographical distribution of convection. Following the earlier analysis by Williams (1994), we associated these changes with local insolation cycles, which are followed (with a lag of about 1 month) by the variability of air temperatures near the Earth's surface. Simulations indicate that average surface air temperature values for 40°S–40°N or 50°S–50°N are characterized by highest and lowest values during the Northern Hemisphere summer and winter, respectively (the asymmetry arising from the latitudinally imbalanced distribution of land over the two hemispheres), which agrees with the PG variation at Vostok. Moreover, the surface air temperature averaged over 40°S–40°N demonstrates a small local minimum in July amid the flat summer maximum, and a somewhat similar pattern is observed for the Vostok fair-weather PG, which further corroborates the idea that the Vostok PG variation reflects the seasonal dynamics of global insolation at low and middle latitudes.

Thus, in Part 1 of this study we have concluded that it is highly likely for the Vostok PG variation (with the highest values during the Northern Hemisphere summer) to be representative of the actual seasonal behavior of the GEC. In this article (Part 2) we shall further investigate the seasonal variation of the GEC using IP simulations in a weather forecasting model and in a climate model (the models and simulation procedures will be described in detail in Section 2). In Section 3 we shall analyze the seasonal variation in terms of regional contributions to the IP on the basis of simulations; in particular, we will further elaborate the discussion of surface air temperature patterns outlined above. In Section 4 we will discuss how one can improve the IP parameterization in order to make the agreement between simulations and observations better.

2. Methods and Data

In this section we describe the data which we shall use below for further analysis of the seasonal behavior of the GEC. We shall employ two different approaches:

1. Simulation of the IP using the weather forecasting model WRF (Weather Research and Forecasting model) on the basis of meteorological reanalysis data;
2. Simulation of the IP using the climate model INMCM (Institute of Numerical Mathematics Climate Model) without explicitly using the results of meteorological observations.

The details of both models will be described below, but first we shall discuss the general approach to simulating the IP in models of atmospheric dynamics.

2.1. Parameterization of the IP

Let z be the altitude above sea level. Suppose that the atmosphere is somehow divided into a number of one-dimensional vertical columns such that the nth column is characterized by the conductivity profile $\sigma_n(z)$ and the vertical source current density profile $j_n^s(z)$ (this quantity represents charge separation inside electrified clouds and is equal to zero outside them). Then the IP V can be approximated by the following formula:

$$V = \sum_n S_n \int_0^{h_{\max}} \frac{j_n^s(z)\,dz}{\sigma_n(z)} \left(\int_0^{h_{\max}} \frac{dz}{\sigma_n(z)} \right)^{-1} \Bigg/ \sum_n S_n \left(\int_0^{h_{\max}} \frac{dz}{\sigma_n(z)} \right)^{-1}, \tag{1}$$

where $h_{\max}$ is the height of the outer boundary of our model of the atmosphere (in practical computations one can take $h_{\max} \sim 70$ km) and S_n is the area covered by the nth column (for more details, see Part 1 of this study). Equation 1 is a general equation valid for any partition of the atmosphere into columns as long as we assume the problem in each column essentially one-dimensional (cf. Slyunyaev et al., 2014); the formula actually follows from the balance of currents driven upward by charge separation inside electrified clouds and currents flowing downward in fair-weather regions.

To estimate IP values in simulations of atmospheric dynamics (both with the WRF and with the INMCM), we use a parameterization based on Equation 1. For any model of atmospheric dynamics, we consider grid columns over cells of the latitude-longitude grid of the model; let $\tilde{S}_i$ be the total surface area of the ith such grid column. We suppose that each grid column is divided into two subcolumns, one of which is completely covered by electrified clouds and the other is not covered by such clouds at all (we can regard it as "fair-weather"). If α_i denotes the portion of the ith grid column covered by electrified clouds, then the two subcolumns have surface areas $\alpha_i\tilde{S}_i$ and $(1 - \alpha_i)\tilde{S}_i$, respectively ($\alpha_i = 1$ indicates that the ith grid column is entirely covered by electrified clouds, whereas $\alpha_i = 0$ means that the grid column is purely fair-weather).

Now we apply general Equation 1 to the partition of the atmosphere into subcolumns of grid columns described above. First of all, we assume a uniform exponential conductivity profile in the entire atmosphere: $\sigma(z) = \sigma_0 \exp(z/H)$, where σ_0 is the conductivity value at the Earth's surface and H is a scale height; based on more elaborate conductivity parameterizations (e.g., Tinsley & Zhou, 2006), in calculations one can take $\sigma_0 \sim 50$ fSm/m and $H \sim 5$–6 km. Of course, such an assumption simplifies the real situation, not taking into account possible effects of radon and aerosols near the Earth's surface, as well as conductivity reduction inside nonelectrified and electrified clouds (note, however, that in electrified clouds the attachment of ions to hydrometeors, causing this reduction, may be counterbalanced by additional ionization owing to corona discharges from ice hydrometeors). However, as shown by Ilin et al. (2020), taking these effects into consideration should not substantially affect simulated trends and patterns in IP variation, and a universal exponential conductivity profile appears to be a decent approximation. Substituting the exponential conductivity profile into Equation 1 gives the following:

$$V = \sum_n \frac{S_n}{S_\mathrm{E}} \int_0^{h_\mathrm{max}} \frac{j_n^\mathrm{s}(z)\,dz}{\sigma(z)}, \tag{2}$$

where S_E is the total area of the Earth's surface and the summation takes place over all our subcolumns of grid columns.

Next, we assume the vertical source current density $j_n^\mathrm{s}(z)$ to be equal to some constant j_0 inside electrified clouds (in the subcolumns occupied by electrified clouds) and equal to zero otherwise. In other words, we assume the same value of the source current density for all electrified clouds; this appears to be reasonable as the simplest approximation, seeing that in simulations we cannot directly distinguish between different types of such clouds. Then Equation 2 yields the following:

$$V = \sum_i \frac{\alpha_i\tilde{S}_i}{S_\mathrm{E}} \int_{z_i^\mathrm{l}}^{z_i^\mathrm{u}} \frac{j_0\,dz}{\sigma(z)} = \sum_i \frac{j_0 H \alpha_i \tilde{S}_i}{\sigma_0 S_\mathrm{E}} \left(\exp\left(-\frac{z_i^\mathrm{l}}{H}\right) - \exp\left(-\frac{z_i^\mathrm{u}}{H}\right) \right), \tag{3}$$

where the sum is taken over all model grid columns, and for the ith such column z_i^l and z_i^u indicate the lower and upper boundaries of the mixed phase region inside electrified clouds (for this is precisely the region where charge separation occurs). Note once again that $\tilde{S}_i$ in Equation 3 is not exactly the same as S_n in Equation 2: $\tilde{S}_i$ in Equation 3 is the surface area covered by the ith column of the model grid, whereas S_n in Equation 2 is the surface area covered by the nth column in our partition of the atmosphere into smaller subcolumns (with two subcolumns making up each grid column; thus for each n there is such i that $S_n = \alpha_i\tilde{S}_i$ or $S_n = (1 - \alpha_i)\tilde{S}_i$).

We associate electrified clouds with deep convection (not taking into account the so-called Austausch mechanism, describing a vertical transport of space charge by convection in the boundary layer) and single out such grid columns by demanding that the value ε_i characterizing convective available potential energy (CAPE) in the column exceed some threshold value ε_0. Thus, for the grid columns with $\varepsilon_i < \varepsilon_0$ we assume that $\alpha_i = 0$; for other grid columns, following the idea first suggested by Mareev and Volodin (2014), we assume that α_i is proportional to the ratio of the amount of convective precipitation totaled over the preceding hour P_i to the total amount of precipitable water W_i, that is, $\alpha_i = kP_i/W_i$ with some constant coefficient k (this assumption is motivated by considering the ascent of precipitating air parcels driven upward by convection; for more details, see Ilin et al., 2020). In other words, we assume that

$$\alpha_i = \begin{cases} kP_i/W_i, & \varepsilon_i \geq \varepsilon_0, \\ 0, & \text{otherwise;} \end{cases}$$

substituting this in Equation 3, we finally arrive at the following parameterization of the IP:

$$V = \sum_i \frac{j_0 k H \tilde{S}_i}{\sigma_0 S_{\mathrm{E}}} \frac{P_i}{W_i} \left(\exp\left(-\frac{z_i^{\mathrm{l}}}{H}\right) - \exp\left(-\frac{z_i^{\mathrm{u}}}{H}\right) \right) \times \begin{cases} 1, & \varepsilon_i \geq \varepsilon_0, \\ 0, & \text{otherwise,} \end{cases}$$

or, considering that constant coefficients do not matter as long as we focus on relative changes in V or relative contributions to V,

$$V \propto \sum_i \frac{\tilde{S}_i P_i}{W_i} \left(\exp\left(-\frac{z_i^{\mathrm{l}}}{H}\right) - \exp\left(-\frac{z_i^{\mathrm{u}}}{H}\right) \right) \times \begin{cases} 1, & \varepsilon_i \geq \varepsilon_0, \\ 0, & \text{otherwise.} \end{cases} \quad (4)$$

In calculations we approximate z_i^{l} and z_i^{u} by the heights of the 0°C and −38°C isotherms, respectively; we also assume $H = 6$ km, and we set ε_0 equal to 0.6, 0.8, 1, or 1.2 kJ/kg (each of these four possibilities will be considered below, since the results of our simulations will turn out to be sensitive to the choice of ε_0). To study regional contributions to the IP, we just restrict the summation in Equation 4 to the grid columns corresponding to specific regions of the Earth's surface. Further discussion of this parameterization can be found in Ilin et al. (2020); the only slight difference here is that now we total convective precipitation over the preceding 1-hr interval rather than over a symmetric 2-hr interval around the moment in question (our analysis has shown that this modification gives a slightly better agreement of simulations with measurements).

2.2. Simulating the IP With the WRF Model

One possible approach to simulating the variation of the GEC is to reproduce the atmospheric dynamics for some period of time on the basis of actual meteorological data and then estimate the IP by means of a parameterization similar to Equation 4. Following this approach, we used the weather forecasting model WRF (see, e.g., Powers et al., 2017; Skamarock et al., 2019) to simulate the atmospheric dynamics during 1980–2020, using ERA5 (fifth generation European Centre for Medium-Range Weather Forecasts reanalysis) meteorological reanalysis data (Hersbach et al., 2023) as initial conditions in model runs. The simulations were performed on a $1° \times 1°$ latitude-longitude grid for every third day; during each model run we estimated hourly values of P_i, W_i, z_i^{l}, z_i^{u}, and ε_i in each column (the last quantity calculated using the cape_2d function from the wrf-python package; see Ladwig, 2017) and then inferred grid cell contributions to the IP by repeatedly applying Equation 4. The computations were performed four times for four different values of ε_0 that we consider; for convenience of presentation, in each case we normalized the resulting values by demanding that the global mean value of the IP over 1980–2020 be equal to 240 kV (Markson, 2007). Other technical details and exact procedures used to process the simulation results are described in Supporting Information S1.

2.3. Simulating the IP With the INMCM Model

An alternative approach to simulating the variation of the GEC is to employ a long-term free run of a climate model without any nudging based on the results of meteorological observations. For this study, we attempted simulating the atmospheric dynamics with the help of the climate model INMCM (Volodin, 2023). The atmospheric part of the INMCM uses a $1.5° \times 2°$ latitude-longitude grid; for the purpose of this study, the model was run to continuously simulate 42 years of modern climate, starting with the year 1979 (as before with the WRF, here we restrict our attention to 1980–2020, although this time simulations are not based on real meteorological data and, by inference, model years do not precisely correspond to actual years). Thus, we obtained hourly values of P_i, W_i, z_i^{l}, z_i^{u}, and ε_i in each atmospheric column (this time we took for ε_i the value of CAPE at the Earth's surface) and then estimated grid cell contributions to the IP via Equation 4. As before, we generated four IP data

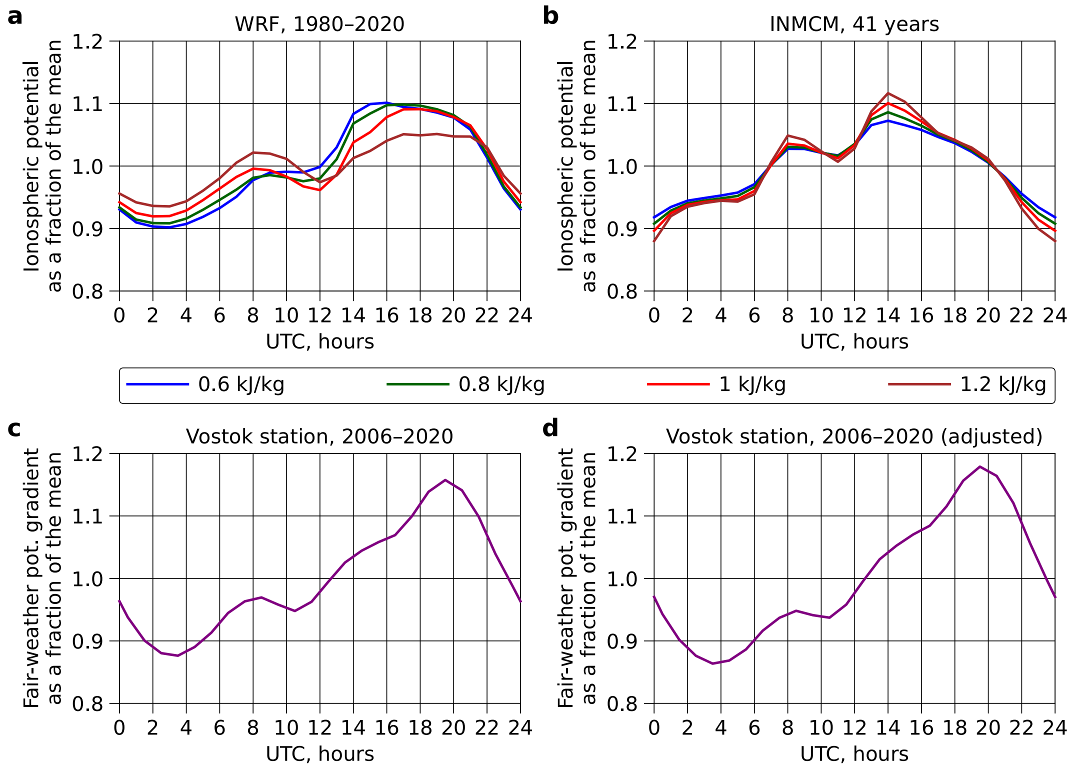

Figure 1. (a) The average diurnal variation of the IP simulated for 1980–2020 using the WRF model. (b) The average diurnal variation of the IP simulated for 41 years approximately corresponding to 1980–2020 using the INMCM model. Different curves in panels (a) and (b) correspond to four different values of the CAPE threshold in the parameterization given by Equation 4, namely 0.6 kJ/kg (blue), 0.8 kJ/kg (green), 1 kJ/kg (red), and 1.2 kJ/kg (brown). (c) The average diurnal variation of the fair-weather PG according to measurements at the Vostok station in 2006–2020. (d) The same as (c) for the fair-weather PG adjusted for local meteorological and solar wind influences.

sets for four different values of ε_0 and in each case normalized the resulting IP values by setting the global mean over 1980–2020 equal to 240 kV. Other technical details are given in Supporting Information S1.

2.4. Other Data

Apart from the results of simulations described above, in some discussions below we shall consider the data used in Part 1 of this study. These data include the results of surface PG measurements at Vostok station in Antarctica during 2006–2020 and surface air temperature values simulated with the WRF during the model runs described in Section 2.2 (we identify surface air temperature with air temperature at 2 m above the ground).

3. Results and Their Analysis

Now we will analyze the seasonal variation of the GEC using the two data sets described in the previous section (the IP simulated with the WRF model for 1980–2020 and the IP simulated with the INMCM model for 41 years that roughly correspond to the same period of 1980–2020).

3.1. On the Choice of CAPE Thresholds to Cut Off Shallow Convection

When simulating the IP, we use four different values of the CAPE threshold ε_0 in Equation 4, namely 0.6, 0.8, 1, or 1.2 kJ/kg. The choice of ε_0 close to 1 kJ/kg in our parameterization was originally motivated by requiring the simulated diurnal variation of the IP to resemble the classical Carnegie curve, but the exact value was not very important since all ε_0s in some neighborhood of 1 kJ/kg yielded diurnal cycles with more or less the same shape (see Ilin et al., 2020, Figure 4d). To illustrate this, in Figures 1a and 1b we show the average diurnal variation curves derived from WRF and INMCM simulations for 1980–2020 with the four different values of ε_0. To assess the quality of simulations, in Figure 1c we demonstrate a diurnal variation of the fair-weather surface PG at the

Vostok station and in Figure 1d we demonstrate a similar variation based on the same PG data adjusted for local meteorological and solar wind influences (for more details, see Supporting Information S1); here the adjustments only slightly change the magnitude of the variation.

Comparing the IP variation curves obtained with the WRF with the Vostok PG variations, we observe the well-known fact that large-scale simulations are able to correctly reproduce the shape of the diurnal variation of the GEC but generally underestimate its peak-to-peak amplitude (e.g., Ilin et al., 2020). In Figure 1a, we clearly see that $\varepsilon_0 = 1$ kJ/kg gives the most realistic diurnal variation curve: With lower CAPE thresholds the main maximum shifts to earlier hours, and with higher CAPE thresholds the peak-to-peak amplitude becomes even smaller; however, the general shape of the curve still remains more or less the same. The diurnal variation curves simulated with the INMCM (Figure 1b) are less similar to the results of observations (which perhaps should not be surprising in view of the coarser grid); here the amplitude of the variation gradually increases with increasing ε_0, whereas its shape remains the same, and it is difficult to say which value of ε_0 gives the best agreement with observations.

Thus simulations with each model predict generally similar IP diurnal variation curves for different values of ε_0 in the range of 0.6–1.2 kJ/kg. For the seasonal variation of the GEC, however, it turns out that even slight changes in this parameter may affect the results; this should not be surprising in view of the fact that the seasonal behavior of the GEC is subtler than its diurnal behavior, as we will demonstrate below. Therefore in this study we will consider seasonal variation patterns corresponding to several different values of ε_0.

One should be very careful when comparing CAPE values computed in different models of atmospheric dynamics and using different methods. Similar to earlier papers employing the same IP parameterization (e.g., Ilin et al., 2020), in the case of the WRF we use the standard cape_2d function from the wrf-python package (Ladwig, 2017); this function computes CAPE for the air parcel with the highest equivalent potential temperature θ_e within the lowest 3 km. The INMCM, however, computes CAPE values for air parcels at the Earth's surface and also uses a coarser grid compared to the WRF. It is not surprising, therefore, that the distributions of our CAPE values for the two models are somewhat different. Such distributions based on hourly CAPE values in the grid columns lying within 30°S–30°N in our simulations for 1980–2020 are demonstrated in Figure S1a of the Supporting Information S1; when plotting these distributions, we did not take into account the variation of $1° \times 1°$ grid cell areas within this region, for it becomes important only near the poles. One clearly sees that the two distributions are generally similar, showing high percentage of small CAPE values (beyond the limits of the figure), then a minimum around 0.3–0.5 kJ/kg, and finally a maximum around 0.8–1 kJ/kg. However, the positions and shapes of these extrema for the two models are somewhat different.

When selecting the CAPE threshold ε_0 in Equation 4, we cut off grid cells with CAPE lower than ε_0. It is clear that the same value of ε_0 may cut off somewhat different parts of the entire range of grid cells depending on the model and CAPE calculation method. However, if we compare specifically the distributions of maximum θ_e CAPE for the WRF and surface CAPE for the INMCM, we observe that their maxima are not very far from each other, which means that the values of ε_0 within about 0.5–1.3 kJ/kg have more or less similar meanings. This becomes even more clear if we restrict our attention only to grid columns and hours with nonzero precipitation, for such grid columns alone contribute to the IP, according to our parameterization given by Equation 4. The corresponding distributions of CAPE values are shown in Figure S1b of the Supporting Information S1; here maximum θ_e CAPE for the WRF and surface CAPE for the INMCM indeed behave in more or less the same way within the range of 0.5–1.3 kJ/kg.

In view of these observations, in this study we use the same values of ε_0 (0.6, 0.8, 1, and 1.2 kJ/kg) for both the WRF (with maximum θ_e CAPE) and the INMCM (with surface CAPE). This is sufficient for investigating the dependence of simulated IP variations on ε_0 for each model, and in both cases the range between 0.6 and 1.2 kJ/kg corresponds to more or less the same part of the entire CAPE distribution.

3.2. Seasonal Variation According to Simulations

Figures 2a–2d show the seasonal variation of the IP according to our simulations for 1980–2020 with the WRF; each panel corresponds to a specific value of the CAPE threshold ε_0. We observe that for $\varepsilon_0 = 1$ kJ/kg and $\varepsilon_0 = 1.2$ kJ/kg simulations with the WRF generally predict a variation with the main maximum in April, a secondary maximum in November, and two minima in February and August. For $\varepsilon_0 = 0.8$ kJ/kg the pattern is

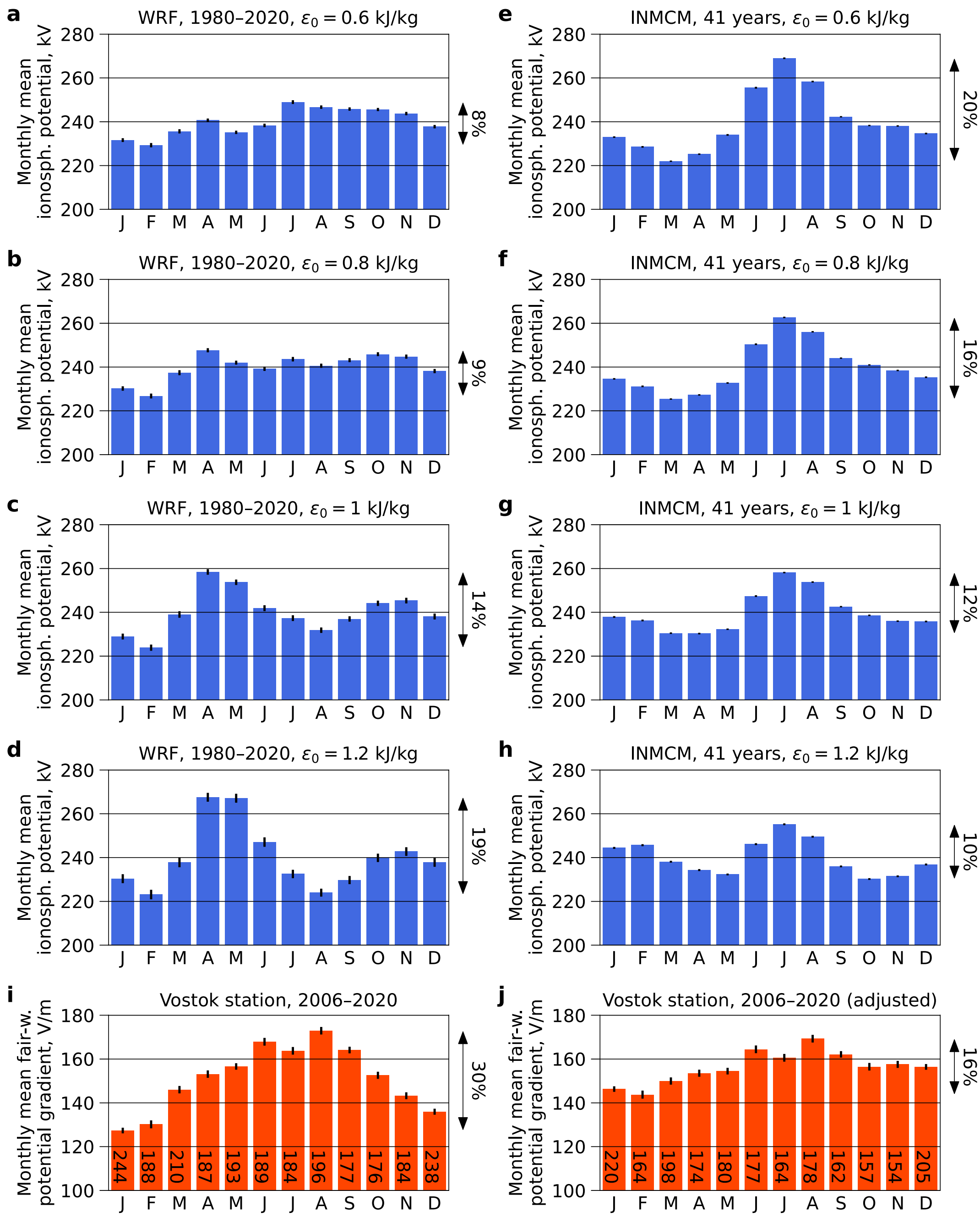

Figure 2. (a)–(d) Monthly mean values of the IP simulated for 1980–2020 using the WRF model. (e)–(h) Monthly mean values of the IP simulated for 41 years approximately corresponding to 1980–2020 using the INMCM model. Different panels correspond to four different values of the CAPE threshold in the parameterization given by Equation 4, namely 0.6 kJ/kg (a, e), 0.8 kJ/kg (b, f), 1 kJ/kg (c, g), and 1.2 kJ/kg (d, h). The shape of the simulated seasonal variation appears to strongly depend on the chosen CAPE threshold and on the model itself. (i) Monthly mean values of the fair-weather PG according to measurements at the Vostok station in 2006–2020 (adapted from Part 1 of this study). (j) The same as (i) for the fair-weather PG adjusted for local meteorological and solar wind influences (adapted from Part 1 of this study). Annotations inside the bars in panels (i) and (j) indicate the number of fair-weather days used to calculate the average values. Error bars in all panels demonstrate the values plus and minus one standard error. The double arrow to the right of each panel represents the peak-to-peak amplitude, and the number next to it gives this amplitude as a fraction of the annual mean.

slightly less clear: We still have the lowest IP value in February and the highest IP value in April, but the secondary maximum shifts to October and there is an inconspicuous local maximum in July. Finally, for $\varepsilon_0 = 0.6$ kJ/kg this July maximum becomes the main one, whereas the April maximum becomes less pronounced; the February value still remains the lowest. In other words, for relatively high values of ε_0 simulations with the WRF generally predict a semiannual periodicity in the GEC intensity with two maxima in April–May and in October–November, whereas for lower ε_0s this semiannual pattern gradually transforms into a variation with an annual periodicity reaching a maximum in July. The peak-to-peak amplitude of the variation substantially increases with increasing ε_0, from 8% of the mean for $\varepsilon_0 = 0.6$ kJ/kg to 19% of the mean for $\varepsilon_0 = 1.2$ kJ/kg.

The seasonal variation of the IP inferred from 41-year simulations with the INMCM is demonstrated in Figures 2e–2h; as before with the WRF, different panels correspond to different ε_0s. For $\varepsilon_0 = 0.6$ kJ/kg and $\varepsilon_0 = 0.8$ kJ/kg simulations with the INMCM predict a variation with a single pronounced maximum in July and a single minimum in March. When we turn to $\varepsilon_0 = 1$ kJ/kg and $\varepsilon_0 = 1.2$ kJ/kg, the July maximum becomes smaller, a secondary maximum in January–February gradually emerges, and the two minima between them eventually move to May and October. Thus simulations with the INMCM predict a distinct annual signal in the seasonal cycle of the GEC with a pronounced maximum during the Northern Hemisphere summer (around July); however, as ε_0 increases, a second maximum appears in January–February, and the semiannual component of the variation becomes more pronounced. The peak-to-peak amplitude varies from 10% of the mean in the case where $\varepsilon_0 = 1.2$ kJ/kg to 20% of the mean in the case where $\varepsilon_0 = 0.6$ kJ/kg.

Comparing Figures 2a–2d with Figures 2e–2h, we conclude that the two models which we consider predict rather different seasonal behavior of the GEC despite the same IP parameterization being used. In both cases the variations tend to have one maximum during the Northern Hemisphere summer for small values of the CAPE threshold ε_0 and two distinct maxima for larger values of ε_0; however, although in the case of simulations with the INMCM these two maxima roughly correspond to the Northern Hemisphere summer and winter, for simulations with the WRF they can be associated with spring and autumn (while summer and winter correspond to minima). We will discuss the origin of this phase difference in more detail below; as for now, we just note that from the perspective of simulations, seasonal variability of the GEC is very sensitive to the details of the IP parameterization (and even to the choice of the model)—much more sensitive than the diurnal variation.

What is more, most of the seasonal patterns described above are different from the variation following from PG measurements at the Vostok station. Figure 2i reproduces the seasonal cycle obtained in Part 1 of this study on the basis of the Vostok fair-weather PG data for 2006–2020. Here the lowest values are reached in January–February and the highest values are reached in June–August, with a small local minimum in July; the peak-to-peak amplitude is about 30% of the annual mean. Note that this amplitude becomes much smaller (reducing to just 16%) if we correct Vostok PG values for the influence of local meteorological variability and solar wind imposed potential differences, which appears to be reasonable; the resulting variation is shown in Figure 2j. We will discuss the cause of a discrepancy between measurements and simulations below.

3.3. Decomposition of Seasonal Variation for the Simulated IP

We have just inferred from Figures 2a–2h that the simulated seasonal variation of the GEC may substantially depend on the details of the IP parameterization and even on the underlying model of atmospheric dynamics. In order to better understand what actually happens here, we recall that simulations (unlike measurements) allow us to look at the behavior of regional contributions to the GEC.

3.3.1. Seasonal Behavior of Surface Air Temperature

Adlerman and Williams (1996) noted that seasonal changes in deep convection (and, by inference, in the occurrence of electrified clouds) are largely governed by the variability of insolation, which has two equinoctial maxima in the tropics and a pronounced local summer maximum outside the tropical belt. Williams (1994) pointed out that surface air temperature often behaves in more or less the same fashion as insolation with a lag of about 1 month. In Part 1 of this study we employed surface air temperatures simulated with the WRF to interpret the seasonal variation patterns following from the Vostok PG data (shown in Figures 2i and 2j). It will be convenient for us to begin our discussion of regional contributions by analyzing the behavior of surface air temperature in more detail—once again on the basis of our simulations of atmospheric dynamics for 1980–2020 with the WRF. In the context of the WRF data, by surface air temperatures we always mean simulated temperatures at 2 m above the ground.

Figure 3a shows monthly mean values of the surface air temperature averaged over each 1° wide circle of latitude between 30°S and 30°N (i.e. 29°S–30°S, 28°S–29°S, and so on up to 29°N–30°N); in other words, this figure shows surface air temperature as a function of month and latitude. Horizontal cross-sections of Figure 3a represent annual cycles of temperature at specific latitudes; for example, around 30°S and 30°N we observe a temperature variation with a prominent maximum during the local summer and a prominent minimum during the local winter, whereas near the equator (0°) the variation appears to have two maxima in spring and autumn (although it is difficult to see them clearly in this panel, as the amplitude of the variation is rather small).

Figure 3b demonstrates the seasonal variation of the surface air temperature values averaged over several relatively small latitude ranges. We subdivide the 30°S–30°N belt into six smaller regions, separated by circles of latitude at 18°S, 9°S, 0°, 9°N, and 18°N. These boundaries are deliberately chosen to be multiples of 3° in order for the regions to consist of entire grid cells for both 1° × 1° WRF and 1.5° × 2° INMCM simulations, considering that later we shall compare temperature variability with that of contributions to the IP according to these two models. The six regions are shown in Figure 3g with the same colors that have been used for different bar charts of Figure 3b.

Let us first discuss the temperature variation in the Northern Hemisphere. For the latitude range of 0°–9°N (light orange bars in Figure 3b) we see a variation with two maxima in April–May and in October–November, of which the former is larger than the latter. These two maxima evidently mirror the two equinoctial maxima in tropical insolation, albeit with a lag of about 1 month. As we pass to higher latitudes within the tropics, namely to 9°N–18°N (light olive bars), the two maxima in air temperature become closer to each other, and in the region between 18°N and 30°N (olive bars) they merge into a single pronounced maximum in July–August, which apparently reflects the solstitial maximum of the insolation cycle in the Northern Hemisphere outside the tropics, once again with a 1 month lag.

For the Southern Hemisphere, the situation is somewhat different. In the 0°–9°S latitude range (orange bars in Figure 3b) the surface air temperature variation is quite similar to that for 0°–9°N, but the main maximum shifts to March–April and the second maximum is no longer present, turning into a sort of plateau from November to January. In the more southern tropical region of 9°S–18°S (light cyan bars) we already see a single prominent maximum in February–March, and in the region between 18°S and 30°S (cyan bars) this maximum shifts to January–February, that is, about 1 month behind the solstitial maximum of insolation in the mid-latitude Southern Hemisphere.

Looking at different bar plots of Figure 3b, we immediately observe that the variation of surface air temperature does not simply follow the local annual cycle of insolation. There is an asymmetry between the two hemispheres both in the temperature variation patterns and in their magnitude: For example, two distinct maxima are seen only to the north of the equator, and the peak-to-peak amplitude outside the tropics is greater in the Northern Hemisphere. This asymmetry apparently arises from the latitudinally imbalanced distribution of land and ocean across the two hemispheres, for it is known that the ocean is less responsive to changes in insolation than land areas.

To provide a physical interpretation for the PG variation at Vostok, in Part 1 of this study we looked at the average temperature over different symmetric latitude ranges around the equator. Figure 4 reproduces the variation cycles obtained there, and it will be instructive to discuss them more thoroughly in the present context. Figure 4a shows the monthly mean values of the surface air temperature averaged over the region lying between 20°S and 20°N. We observe two maxima in April–May and in October–November (the former being larger than the latter), which means that the equatorial temperature pattern (see the bar plots for 0°–9°N and 0°–9°S in Figure 3b) dominates the average variation, whereas patterns corresponding to higher tropical latitudes (see the bar plots for 9°N–18°N and 9°S–18°S in Figure 3b) compensate for each other.

Figure 4b is the counterpart of Figure 4a for the region lying between 30°S and 30°N. We observe more or less the same behavior with two maxima following the equinoxes, except that now the second maximum shifts to September–October, and the valley between the two maxima becomes shallower. As we turn to a broader region of 40°S–40°N, the two maxima become even more close to each other; they occur in May–June and in August, with a small local minimum in July separating them (see Figure 4c; in Part 1 we noted that a similar minimum is

10.1029/2024JD042634

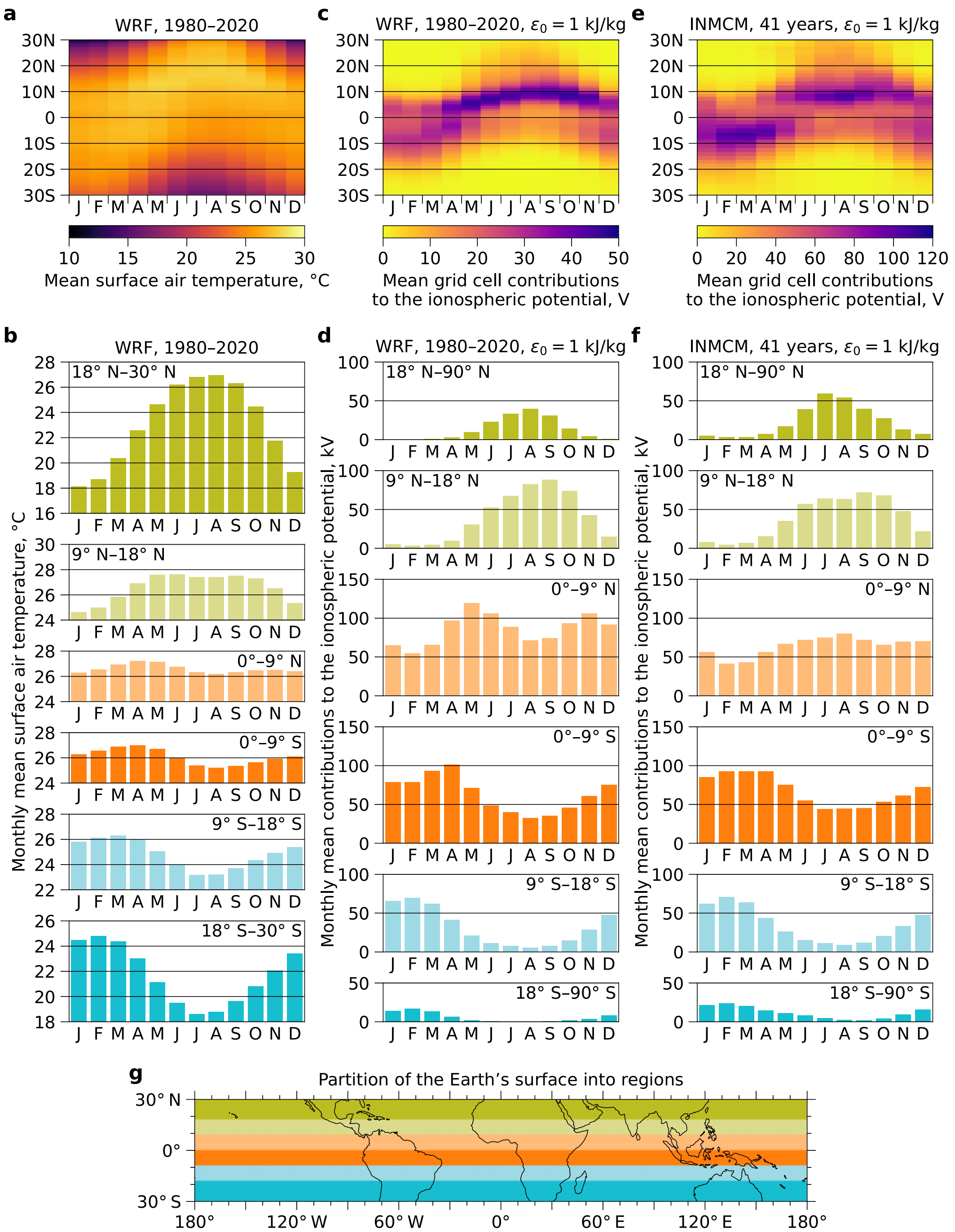

Figure 3. (a) Monthly mean values of air temperature at 2 m above the ground simulated for 1980–2020 using the WRF model and averaged over each 1° wide circle of latitude between 30°S and 30°N. (b) Monthly mean values of the same temperature averaged over six separate regions (18°N–30°N, 9°N–18°N, 0°–9°N, 0°–9°S, 9°S–18°S, and 18°S–30°S). (c) Monthly mean values of 1° × 1° grid cell contributions to the IP simulated for 1980–2020 with the WRF model and averaged over each 1° wide circle of latitude between 30°S and 30°N. (d) Monthly mean values of the same contributions totaled over six separate regions (18°N–90°N, 9°N–18°N, 0°–9°N, 0°–9°S, 9°S–18°S, and 18°S–90°S). (e) Monthly mean values of 1.5° × 2° grid cell contributions to the IP simulated for 41 years approximately corresponding to 1980–2020 with the INMCM model and averaged over each 1.5° wide circle of latitude between 30°S and 30°N. (f) Monthly mean values of the same contributions totaled over six separate regions (18°N–90°N, 9°N–18°N, 0°–9°N, 0°–9°S, 9°S–18°S, and 18°S–90°S). The same CAPE threshold of 1 kJ/kg was used for all simulations presented in panels (c)–(f). (g) The corresponding partition of the Earth's surface; the colors in the map correspond to those in panels (b), (d), and (f) (note that in the case of panels (d) and (f) the outer regions extend beyond 30°S and 30°N to the poles).

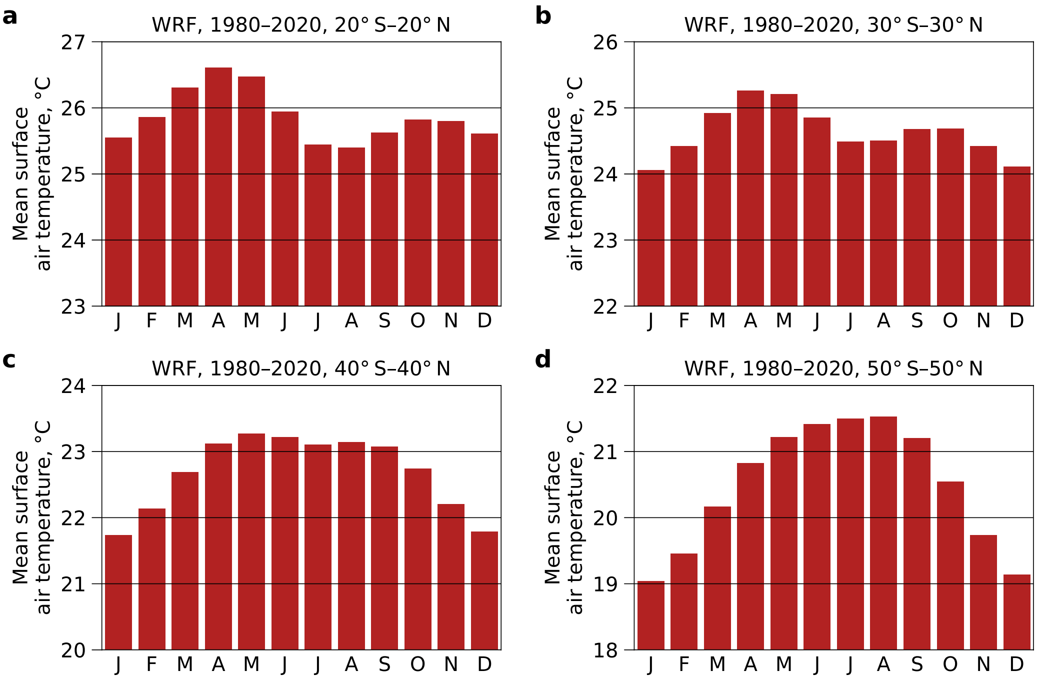

Figure 4. (a)–(d) Monthly mean values of air temperature at 2 m above the ground simulated for 1980–2020 using the WRF model, averaged over different latitude ranges, namely 20°S–20°N (a), 30°S–30°N (b), 40°S–40°N (c), and 50°S–50°N (d). Adapted from Part 1 of this study.

observed in the Vostok PG variation, shown in Figures 2i and 2j). If we average surface air temperature over 50°S–50°N, the two maxima finally merge, and we have a pronounced variation with highest values during the boreal summer, as shown in Figure 4d. Thus for sufficiently wide symmetric latitude ranges around the equator the mean annual variation of surface air temperature is dominated by the Northern Hemisphere. One might have expected this from Figure 3b, which clearly shows that the peak-to-peak amplitude of the mean temperature variation in 18°N–30°N is substantially larger than its counterpart for 18°S–30°S (owing to the greater amount of land in the Northern Hemisphere).

Finally, let us note that the results presented in Figures 4a–4d qualitatively agree with the mean temperature variations for 25°S–25°N and 60°S–60°N plotted by Williams (1994), of which the former had two maxima in April–May and September–October, whereas the latter showed a single pronounced maximum in July–August (see Williams, 1994, Figures 4a and 4c). For our analysis of the GEC variation we will need a more complete picture of seasonal changes in surface air temperature, and that is why we have discussed them in detail with Figures 3a, 3b, and 4 before turning our attention to contributions to the IP.

3.3.2. Seasonal Behavior of Regional Contributions to the Simulated IP

We will now discuss the annual variation of contributions to the IP according to our simulations. In accordance with the discussion of surface air temperatures given above and following earlier analyses by Williams (1994) and Adlerman and Williams (1996), we will primarily focus on how seasonal variation patterns change with latitude. For the time being, we shall consider the results of our simulations for 1980–2020 with the WRF and of our 41-year simulations with the INMCM under the assumption that $\varepsilon_0 = 1$ kJ/kg (see Figures 2c and 2g); other values of the CAPE threshold will be discussed in Section 3.3.3 below.

Similarly to Figure 3a for surface air temperature, Figure 3c demonstrates monthly mean values of $1° \times 1°$ grid cell contributions to the IP at different latitudes, according to our WRF simulations. More precisely, the figure shows the simulated IP values averaged over each 1° wide circle of latitude between 30°S and 30°N (i.e. 29°S–30°S, 28°S–29°S, and so on up to 29°N–30°N). The patterns of variation of contributions to the IP with month and latitude shown in Figure 3c are generally similar to those of temperature shown in Figure 3a, except that significant contributions to the IP are localized in a rather small range of latitudes.

Figure 3e is the counterpart of Figure 3c for our simulations with the INMCM. It shows monthly mean values of $1.5° \times 2°$ grid cell contributions to the IP averaged over 1.5° wide circles of latitude within 30°S–30°N (i.e., 30°S–28.5°S, 28.5°S–27°S, and so on up to 28.5°N–30°N). The patterns of variation are generally similar to those obtained in WRF simulations. Note that owing to different grid cell sizes, typical values of contributions to the IP presented in Figure 3e are greater than those inferred from Figure 3c.

As before with surface air temperature, horizontal cross-sections of Figures 3c and 3e represent the annual behavior of contributions to the GEC at specific latitudes. We immediately see that according to both models, the contribution of latitudes slightly to the north of the equator (say, 0°–5°N) has two maxima after the equinoxes (although their predicted positions depend on the model), whereas for the latitudes around 10°S and 10°N there appears to be a single maximum during the local summer and a single minimum during the local winter. The regions lying beyond the 20°S–20°N range give only a small contribution to the total IP, according to the parameterization which we employ.

Figures 3d and 3f show the seasonal variation of contributions to the IP from several specific latitude ranges according to our simulations with the WRF and with the INMCM, respectively. We use the same partition into six regions that has been employed in Figure 3b, separating them with circles of latitude at 18°S, 9°S, 0°, 9°N, and 18°N (see Figure 3g). The only difference is that now we do not bound the two outer regions by 30°S and 30°N, extending them up to the poles instead; this actually does not matter much, since calculations show that on average, the regions outside the 30°S–30°N range contribute only about 1% of the total IP according to the WRF and about 5% of the total IP according to the INMCM.

By looking at the bar plots shown in Figures 3d and 3f and comparing them with surface air temperature variation presented in Figure 3b, we infer that local temperature cycles at different latitudes are generally reflected by the corresponding contributions to the IP. The most notable difference is that for air temperature the magnitude of the variation (in °C) increases as we move away from the equator, whereas for the simulated contributions to the IP this magnitude (in kV) rapidly decreases.

For the contribution to the GEC from the 0°–9°N latitude range (light orange bars in Figures 3d and 3f) we see two distinct maxima. According to the WRF, these maxima are reached after the equinoxes, in May and November, whereas the INMCM predicts them to be rather flat and occur somewhat later, in May–September (with the highest value reached in August) and November–December. For the southern equatorial region of 0°–9°S (orange bars) the situation is slightly different, as we see only one clear maximum. The WRF predicts it to occur in April, and instead of the second maximum it yields a plateau in December–February; the INMCM predicts a single flat maximum in February–April.

For the regions outside the 9°S–9°N range we obtain a variation of contributions to the GEC with one maximum during the local summer. The only manifestation of the tropical insolation cycle can be seen in the INMCM simulations for 9°N–18°N (light olive bars), where there is a plateau in July–August within a flat June–October maximum with the highest value attained in September; the WRF predicts for this region a more pronounced maximum in August–September. For higher latitudes in the Northern Hemisphere, 18°N–90°N (olive bars), we obtain a single maximum in August (according to the WRF) or in July (according to the INMCM). In the Southern Hemisphere for 9°S–18°S (light cyan bars) and 18°S–90°S (cyan bars) both models predict a single maximum in February.

3.3.3. Interpretation of the Seasonal Variation of the Total Simulated IP

Having discussed seasonal patterns in regional contributions to the GEC depending on the latitude, we now turn to the question as to how these contributions combine to form the variation of the total IP. We will no longer confine ourselves to the case where the CAPE threshold ε_0 in our IP parameterization equals 1 kJ/kg, and will consider other options discussed in Section 3.2 as well, namely the cases of $\varepsilon_0 = 0.6$ kJ/kg, $\varepsilon_0 = 0.8$ kJ/kg, and $\varepsilon_0 = 1.2$ kJ/kg. We have seen before that the simulated variation of the total IP strongly depends on the value of ε_0 and even on our choice of the model (see Figures 2a–2h); now we shall try to explain this fact in terms of regional contributions and find some patterns which would be common for all models and parameterizations.

Figures 5a–5h present the decomposition of the IP variations according to the WRF and INMCM with different values of ε_0 into regional contributions. The eight panels of Figure 5 precisely correspond to the first eight panels of Figure 2, and we consider the same six latitude ranges that were earlier used in Figures 3d and 3f, namely 18°S–

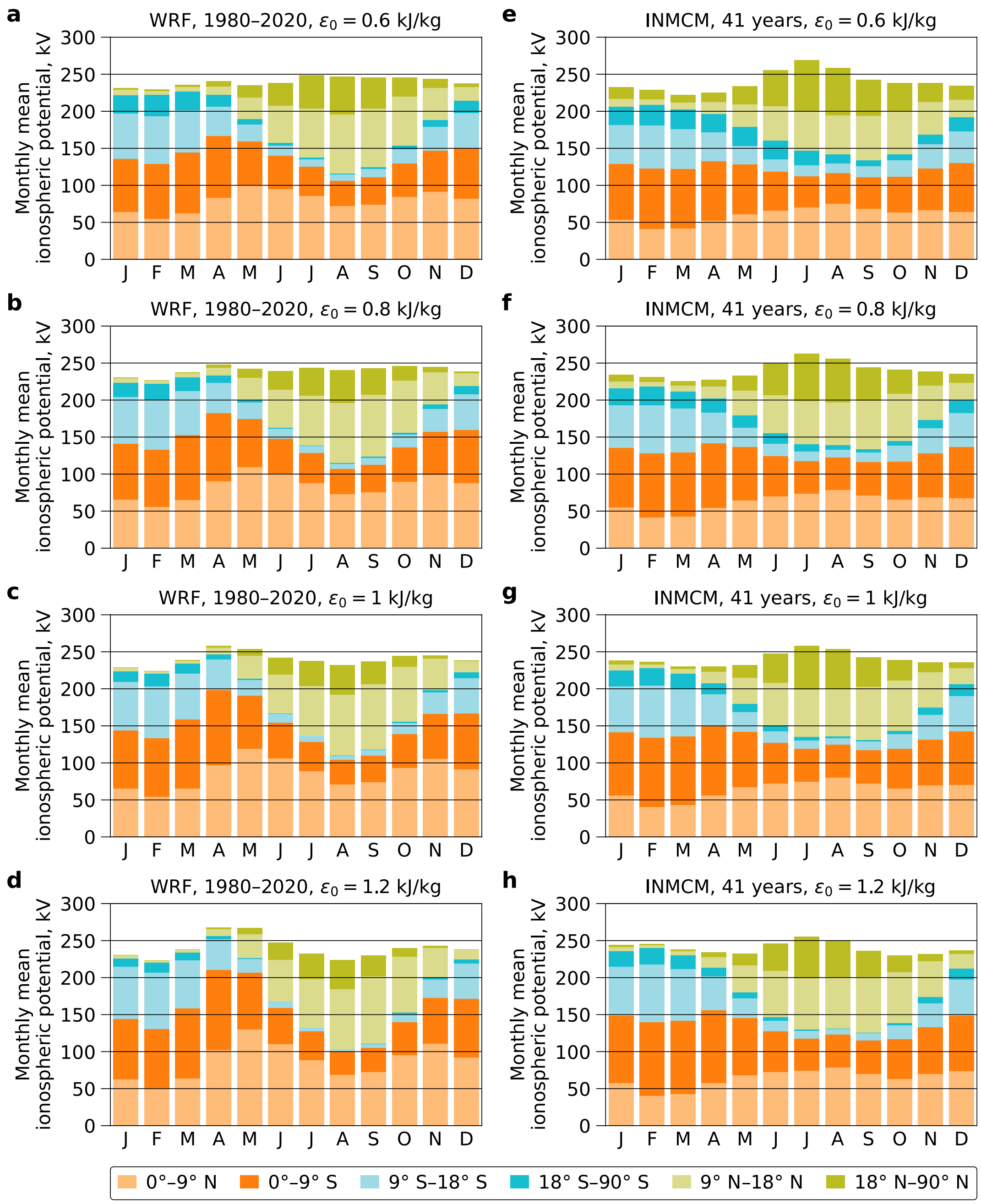

Figure 5. (a)–(h) The simulated IP variations of Figures 2a–2h decomposed into contributions from six separate regions: 0°–9°N, 0°–9°S, 9°S–18°S, 18°S–90°S, 9°N–18°N, and 18°N–90°N (bottom to top). The colors are the same as those in Figure 3g. The contributions presented in panels (c) and (g) are shown separately in Figures 3d and 3f, respectively.

90°S, 9°S–18°S, 0°–9°S, 0°–9°N, 9°N–18°N, and 18°N–90°N (see Figure 3g). In particular, Figures 5c and 5g, corresponding to the parameterization with $\varepsilon_0 = 1$ kJ/kg, are precisely cumulative representations of Figures 3d and 3f, respectively.

Let us first look at the total contribution to the simulated IP from the equatorial belt between 9°S and 9°N. Here we combine together the contributions from 0°–9°S to 0°–9°N, notwithstanding the asymmetry in contributions to the IP near the equator, which we have seen in Figures 3c–3f. The contributions of 0°–9°S and 0°–9°N are indicated in each panel of Figure 5 by shades of orange, and the total contribution of the 9°S–9°N range is their combination. We observe that both the WRF and the INMCM predict for this combined equatorial contribution a variation with two main maxima following the equinoxes regardless of the value of ε_0. The only difference is that the WRF predicts maxima in April and November–December and minima in February and August, whereas according to the INMCM, the main maxima occur in April and December–January and the minima occur in February–March and July–October (with a small local maximum in August inside the latter of them); in other words, the equatorial seasonal cycle predicted by the INMCM follows its WRF counterpart with a lag of about 1 month.

The contributions of the 9°S–18°S and 18°S–90°S ranges are shown in Figure 5 by shades of cyan; their combination represents the total contribution to the IP from the nonequatorial Southern Hemisphere (more precisely, the part of the Southern Hemisphere lying beyond our tropical belt and occupying the latitude range of 9°S–90°S). It is easy to see that this combined contribution reaches highest values in January–March with the maximum in February (i.e., during the austral summer) and is lowest during July–September or August–October with the minimum in August or September. Likewise, the contribution to the IP from the nonequatorial Northern Hemisphere (9°N–90°N) is a combination of contributions from 9°N–18°N to 18°N–90°N, which are indicated in Figure 5 by shades of olive. This contribution behaves oppositely to that of the nonequatorial Southern Hemisphere, being highest in July–September with the maximum in July or August (i.e., during the boreal summer) and lowest in January–March with the minimum in February or March. Note that the general behavior of nonequatorial contributions depends on neither the model nor the value of ε_0.

In view of these observations we can decompose the variation of the total IP as the sum of three rather simple variations of contributions from the equatorial belt (9°S–9°N in our analysis), southern nonequatorial region (9°S–90°S), and northern nonequatorial region (9°N–90°N). The equatorial variation has two maxima following the equinoxes and two minima between them, whereas nonequatorial contributions are highest at the end of the local summer (austral for the Southern Hemisphere and boreal for the Northern Hemisphere) and lowest at the end of the local winter. These variations apparently reflect the local weather and climate dynamics in the respective regions, for we already observed when discussing Figure 3 that the variation of simulated contributions to the GEC reflects the variation of surface air temperature and thus is eventually determined by seasonal changes in insolation. In this connection it is worthy of note that the equatorial type of variation with two maxima takes place only for a small range of latitudes near the equator—much smaller than the entire tropics (which are bounded by 23.4°S and 23.4°N). However, in our simulations this small latitude range may produce a considerable portion of the total IP.

Thus we have represented the seasonal variation of the total IP as the sum of three essentially different individual patterns for 9°S–9°N, 9°S–90°S and 9°N–90°N. When we add up these three patterns, they to a large extent offset each other. The maxima of the equatorial contribution occur after the equinoxes, whereas its minima occur after the solstices and thus coincide with the maxima of nonequatorial contributions. Roughly speaking, the two nonequatorial contributions completely of partially “fill” the two valleys between the equatorial maxima (see Figure 5). The resulting effect is rather subtle and difficult to predict; as we pointed out when discussing Figures 2a–2h, the outcome of simulations depends on the details of the IP parameterization and even on the chosen weather or climate model.

Comparing the simulated variations obtained with different values of the CAPE threshold ε_0 in the IP parameterization, shown in Figure 5, we observe that both the mean value of the equatorial contribution to the IP and the amplitude of its variation increase with increasing ε_0. This is probably not surprising, as higher CAPE thresholds imply greater role of the equatorial tropics, where typical values of CAPE are higher than anywhere else.

In our simulations with the WRF (Figures 5a–5d) the annual mean contribution from 9°S to 9°N gradually increases from 57% of the total IP in the case of $\varepsilon_0 = 0.6$ kJ/kg through 60% in the case of $\varepsilon_0 = 0.8$ kJ/kg and 62% in the case of $\varepsilon_0 = 1$ kJ/kg to 63% in the case of $\varepsilon_0 = 1.2$ kJ/kg. The corresponding change in the peak-to-peak amplitude of the equatorial contribution is much more conspicuous: For 0.6, 0.8, 1, and 1.2 kJ/kg this amplitude amounts to 44%, 52%, 63%, and 73% of the mean, respectively. Thus, according to the WRF, about 60% of the total IP is supplied by the equatorial region, and the annual variation of this contribution is characterized by pronounced maxima. It is therefore clear that the behavior of the total IP shown in Figures 2a–2d (and decomposed in Figures 5a–5d) is to a large extent determined by the equatorial contribution, which explains both the semiannual periodicity with maxima following the equinoxes (except for $\varepsilon_0 = 0.6$ kJ/kg) and the growth of the amplitude of the resulting variation with increasing ε_0.

For simulations with the INMCM (Figures 5e–5h) the situation is somewhat different. The annual mean contribution of the 9°S–9°N range still slightly increases with increasing ε_0, changing from 51% of the total IP at $\varepsilon_0 = 0.6$ kJ/kg through 53% at $\varepsilon_0 = 0.8$ kJ/kg and 55% at $\varepsilon_0 = 1$ kJ/kg to 56% at $\varepsilon_0 = 1.2$ kJ/kg. The peak-to-peak amplitude still shows a more substantial increase: 18%, 20%, 24%, and 30% of the mean for 0.6, 0.8, 1, and 1.2 kJ/kg, respectively. However, considering that the INMCM predicts the equatorial contribution to constitute a lower portion of the total IP and to have less pronounced maxima (compared to the equatorial contribution according to the WRF), the resulting behavior of the total IP shown in Figures 2e–2h (and decomposed in Figures 5e–5h) turns out to be dominated by the two nonequatorial contributions with maxima after the solstices (rather than after the equinoxes). As ε_0 increases, the equatorial contribution counterbalances the nonequatorial ones, and the amplitude of the resulting variation decreases.

Summarizing the above discussion, we conclude that there are clear and pronounced seasonal variation patterns in contributions to the GEC from the equatorial region, the southern nonequatorial region, and the northern nonequatorial region (in our analysis these three regions are separated by the circles of latitude at 9°S and 9°N, but our choice of these boundaries was somewhat arbitrary). The equatorial variation has two maxima occurring after the equinoxes, whereas each of the nonequatorial cycles has a single maximum during the local summer after the solstice. When the three pronounced regional patterns are added up together, they offset each other (the minima of the equatorial cycle are counterbalanced by the maxima of the nonequatorial ones), and the resulting variation of the total IP appears to be much less pronounced than its constituent parts. In simulations the shape of this total variation strongly depends on the model and details of the IP parameterization (even though for each of the three contributions described above the shape of the variation is more or less the same). This explains why it is so difficult to rely on simulations when investigating the seasonal variation of the GEC: Even slight changes in the IP parameterization or the modeling technique may lead to a completely different annual variation of the total IP.

Finally, let us note that equatorial and nonequatorial seasonal patterns, shown in Figures 3d, 3f, and 5a–5h, further support our interpretation of the seasonal behavior of the Vostok PG (Figures 2i and 2j) in terms of insolation, outlined in Part 1 of this study. Indeed, we have just ascertained that contributions to the IP from different latitude ranges are clearly correlated with surface air temperatures and generally reflect local insolation cycles; we have also observed that simulations do not give a definite answer regarding the behavior of the sum of these contributions to the IP. It is thus not unlikely that in reality the nonequatorial patterns prevail over the equatorial one (which, in view of the asymmetry of land distribution, would explain the annual maximum in the GEC intensity during the Northern Hemisphere summer), but some remnants of the equatorial pattern and tropical insolation cycle still survive in the total variation (which would account for the July minimum inside the summer maximum, clearly seen in Figures 2i and 2j).

3.4. The Existence of Stable Seasonal Behavior

In view of the apparent subtlety of the effect of the seasonal cycle of summer and winter on the GEC, it is interesting to investigate whether the simulated patterns of variation discussed above (see Figures 2a–2h) are stable and reproducible. We will confine ourselves to the case where $\varepsilon_0 = 1$ kJ/kg.

We begin with the analysis of the pattern of variation predicted by the WRF (with $\varepsilon_0 = 1$ kJ/kg; see Figure 2c). Figures S2a–S2d in Supporting Information S1 show the monthly mean PG values calculated on the basis of the same data set separately for four individual decades within the whole 1980–2020 period, which yielded the variation of Figure 2c (namely, 1981–1990, 1991–2000, 2001–2010, and 2011–2020; the year 1980 is not taken into account here). We observe that in all of the four cases the IP reaches its main maximum in April or May and has a secondary maximum in October or November; the minima take place in January–February and in August. The peak-to-peak amplitude of the variation does not vary much across the four decades either, and we can conclude that the WRF with our IP parameterization predicts more or less the same annual behavior of the GEC regardless of the time span that we consider (even though the annual mean IP value is slightly different for different decades).

For the seasonal variation pattern predicted by the INMCM (again in the case of $\varepsilon_0 = 1$ kJ/kg; see Figure 2g) the situation is similar. Figure 2g is based on 41 years of climate simulations with the INMCM which roughly correspond to 1980–2020; separate annual cycles of the IP on the basis of years 2–11, 12–21, 22–31, and 32–41 of this model run are demonstrated in Figures S2e–S2h of the Supporting Information S1. We see that the IP variations for different decades are very similar to each other: All of them are characterized by the main maximum in July, a small secondary maximum in December or January, and minima in March or April and in November or December; the amplitude of the variation is also more or less the same.

Let us also recall that in Part 1 of this study we have shown that the seasonal variation curve based on fair-weather PG measurements at Vostok (see Figures 2i and 2j) repeats itself over time. Here we further illustrate this by reproducing "partial" seasonal cycles from Part 1 (based on the Vostok PG data for 2006–2012 and 2013–2020) in Figures S3a and S3b of the Supporting Information S1 and also plotting the same variations adjusted for solar wind and meteorological influences in Figures S3c and S3d of the Supporting Information S1. In each pair the two bar plots are generally similar to each other and to the variations of Figures 2i and 2j; in particular, all of them show a flat summer maximum with a small local minimum inside it (in Part 1 we used this circumstance to draw an analogy between the Vostok PG behavior and the mean surface air temperature cycles of Figures 4c and 4d). Summarizing our inferences from Figures S2 and S3 in Supporting Information S1, we can state that seasonal variation patterns in the GEC intensity, whether simulated or based on measurements, are stable and can be independently reproduced for different sufficiently long time periods (even if the mean values gradually change between these periods). This indirectly supports the idea that there exists a universal average annual variation curve of the GEC.

4. Further Discussion: Toward More Realistic IP Parameterizations for Simulations

Finally, we will discuss whether it is possible to reconcile the results of observations with the results of IP simulations. We have seen that PG measurements at the Vostok station indicate the highest and lowest GEC intensity during the Northern Hemisphere summer and winter, respectively. At the same time our simulations predict very different variation patterns depending on the model and the threshold CAPE value ε_0 in the parameterization given by Equation 4, which expresses the IP in terms of atmospheric variables (see Figures 2a–2h). However, the parameterization based on Equation 4 has its own shortcomings, the most important of which is the apparent underestimation of nonequatorial contributions to the IP for the values of ε_0 close to 1 kJ/kg (at least in the case of the WRF): This underestimation has been pointed out earlier in the context of simulating the diurnal variation of the GEC (Ilin et al., 2020) and studying the effect of the Madden–Julian oscillation on the GEC (Kozlov et al., 2023). At the same time the most realistic diurnal variation curves among those shown in Figure 1a are obtained exactly with ε_0 about 0.8–1 kJ/kg, which makes this range of values preferable. In Section 3.3.3 of this paper, we noted that for WRF simulations with ε_0 of 0.8 kJ/kg or greater the equatorial region lying between 9°S and 9°N already produces more than 60% of the total IP, whereas in reality this relatively small region probably does not account for such a large contribution to the GEC.

It is difficult to say where exactly lies the reason for this underestimation of nonequatorial contributions. In this connection it is interesting to recall that the latitude range between 20° and 40° (in both hemispheres), whose contribution to the IP is likely to be underestimated in our simulations, is characterized by severe convective storms (e.g., Ludlam, 1963, Figure 5; Gertler et al., 2023, Figure 6) and especially high lightning densities (Peterson, 2024, Figure 5); these severe storms are often associated with moist convection downwind of dry terrain (e.g., Emanuel, 2024, Figure 11). Although these extreme events, being not very frequent, are unlikely to determine the average annual dynamics of the IP, their interpretation in terms of moist and dry air suggests a more general explanation for the shortcomings of our parameterization. Indeed, outside the equatorial region the air near the Earth's surface is less moist, and moist convective events are often preceded by dry convection in the relatively high planetary boundary layer. One can hypothesize that during the moist convection phase this may result in more hail and graupel (owing to more intense air entrainment and higher condensation levels) and greater updraft speeds, and the parameterization in terms of CAPE and convective precipitation given by Equation 4 cannot take the corresponding increase of the source current into account. Of course, this is presently only a speculation, and further research in this direction is needed to understand the actual nature of the problem.

When analyzing Figure 5 in Section 3.3.3, we have already noted that the lower contribution of the equatorial region in the case of the INMCM (compared to the WRF) leads to a dominant role of nonequatorial contributions in the seasonal variation, which eventually results in the annual maximum being attained in July (see Figures 5e–5h). We can also mention one earlier result in this direction: Using the same INMCM model and a parameterization similar to that given by Equation 4 but involving a different method of determining deep convection, Mareev and Volodin (2014) obtained an IP variation reaching maximum and minimum values during the Northern Hemisphere summer and winter, respectively (see Mareev & Volodin, 2014, Figure 1b; note, however, that the corresponding diurnal variation showed only a vague similarity to the Carnegie curve, as in our Figure 1b).

Similarly, from Figures 5a–5d we can deduce that the summer minimum in the IP variation according to the WRF becomes less pronounced with decreasing ε_0, when higher latitudes become more important and the equatorial contribution becomes slightly smaller and less variable. For $\varepsilon_0 = 0.6$ kJ/kg, when the equatorial region contributes only 57% of the total IP, we even have a summer maximum (see Figure 5a). This also demonstrates that enhancing the role of nonequatorial contributions would generally lead to the dominance of the northern non-equatorial pattern and higher IP values during the Northern Hemisphere summer and make the shape of the seasonal variation closer to observations. This is consistent with our discussion of surface air temperature plots in Section 3.3.1, where we noted the dominance of the Northern Hemisphere in average variations due to the greater area covered by land to the north of the equator (cf. Williams, 1994).

In order to obtain a better agreement of the simulated seasonal behavior with that known from measurements, we can try to alter the parameterization expressed by Equation 4, taking into account other variables so as to increase the contribution of nonequatorial regions. In doing so, one needs to look not only at the seasonal variation but also at the diurnal cycle, inasmuch as the ability of a parameterization to reproduce the shape of the Carnegie curve (or the shape of the Vostok variation, which is generally the same) is the most basic test of its validity. For example, in the case of the WRF, looking at Figures 5a–5d, we could further reduce the value of ε_0 trying to increase summertime IP values, but it turns out that this would worsen the agreement of the diurnal variation with the Carnegie curve (see Figure 1a). In the remainder of this section we will demonstrate a simple modification of Equation 4 that makes the annual variation closer to observations without affecting the shape of the diurnal variation. We shall focus on simulations with the WRF, as the INMCM is apparently less suitable for reproducing such subtle effects.

Figures 6a and 6b demonstrate the average diurnal and seasonal behavior of the adjusted fair-weather PG at the Vostok station based on measurements made during 2006–2020 (the same plots were earlier shown in Figures 1d and 2j). Figures 6c and 6d show the corresponding variation patterns for the simulated IP in the case of modeling with the WRF and setting $\varepsilon_0 = 1$ kJ/kg in Equation 4. Figure 6d in fact also shows contributions to the total IP from the six latitude ranges earlier considered in Sections 3.3.2 and 3.3.3, thus reproducing Figure 5c (whereas Figure 6c reproduces one of the curves from Figure 1a). Comparing Figures 6a and 6c (both of them present hourly values as fractions of the diurnal mean), we emphasize once again that simulations based on Equation 4 are able to qualitatively reproduce the shape of the diurnal variation of the GEC, although its peak-to-peak amplitude is underestimated (17% of the mean compared to 32% for the PG at Vostok) and the main maximum occurs somewhat earlier. As for the corresponding seasonal cycles, shown in Figures 6b and 6d, we have already noted that simulations and measurements yield rather different variations.

It is noteworthy that, as regards the diurnal variation of the GEC, a certain disagreement of simulations and measurements is very common. All the earlier attempts to estimate the IP in models of atmospheric dynamics in terms of climate variables describing convection produced diurnal variation curves with smaller amplitudes and earlier maxima compared to observations (see Mareev & Volodin, 2014, Figure 1a; Lucas et al., 2015, Figure 7; Jánský et al., 2017, Figure 3a). It appears that when source currents are determined based on variables characterizing convection (such as CAPE or the convective mass flux), the contribution of the tropics is always overestimated; for example, Ilin et al. (2020, Figure 4) have shown that, without taking additional variables into account, no simple modification of the parameterization given by Equation 4 is able to increase the peak-to-peak amplitude of the variation and at the same time retain the correct shape.

We have already noted in Part 1 of this study that the average surface air temperature for 40°S–40°N exhibits a seasonal variation (shown in Figure 4c) which has much in common with the PG variation at Vostok; in addition, regional temperature variation patterns (Figure 3b) are visually similar to those of the corresponding contributions to the IP simulated using our parameterization (Figures 3d and 3f). However, functions of surface air temperature cannot give us a good proxy for the IP: Despite being able to produce the seasonal pattern similar to the one inferred from the Vostok data, temperature does not manifest a diurnal variation similar to the Carnegie curve even in the tropics. Taking this observation into account, we will try to modify the parameterization of Equation 4 by combining surface air temperature data with parameters of convection.

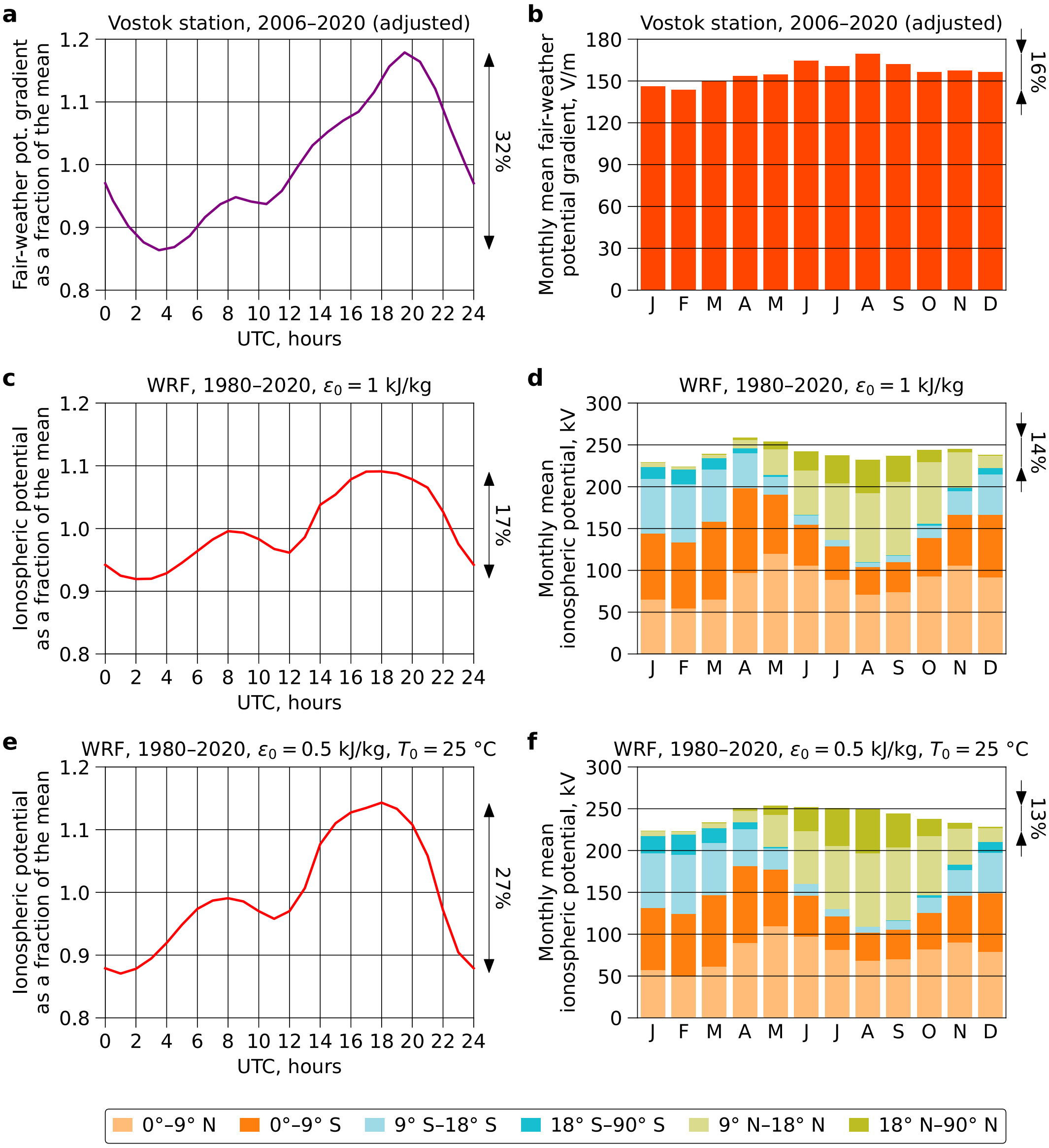

Figure 6. (a), (b) The diurnal variation (a) and monthly mean values (b) of the fair-weather PG according to measurements at the Vostok station in 2006–2020; PG values have been adjusted for local meteorological and solar wind influences. (c), (d) The diurnal variation (c) and monthly mean values (d) of the IP simulated for 1980–2020 using the WRF model and the parameterization given by Equation 4 with the CAPE threshold of 1 kJ/kg. (e), (f) The diurnal variation (e) and monthly mean values (f) of the IP simulated for 1980–2020 using the WRF model and the parameterization given by Equation 5 with the CAPE threshold of 0.5 kJ/kg and the temperature threshold of 25°C. In panels (a), (c), and (e) hourly PG and IP values are presented as fractions of their respective diurnal means. In panels (d) and (f) the seasonal variation of the simulated IP is decomposed into contributions from six separate regions: 0°–9°N, 0°–9°S, 9°S–18°S, 18°S–90°S, 9°N–18°N, and 18°N–90°N (bottom to top). The colors are the same as those in Figures 3g and 5a–5h. The double arrow to the right of each panel represents the peak-to-peak amplitude, and the number next to it gives this amplitude as a fraction of the diurnal or annual mean.

First of all, we will retain cutting off shallow convection by considering only those grid columns where the characteristic value of CAPE ε_i exceeds the threshold value ε_0. At the same time we shall use a smaller value of ε_0 in order to increase the role of higher latitudes. In addition, we will make the source current density j_i inside electrified clouds in the ith grid column (which was assumed equal to a constant j_0 when we derived Equation 4) linearly depend on the surface air temperature T_i in that column. More precisely, we will make it proportional to $T_i - T_0$ provided that $T_i \geq T_0$, where T_0 is some threshold value for air temperature, and we will cut off the grid columns with $T_i < T_0$. This idea is motivated by the fact that we want to more explicitly take into account local insolation cycles and produce an IP variation similar to the temperature variation of Figure 4c, but we also need to exclude the regions with low surface air temperatures, which are unlikely to contribute anything to the GEC. Thus, instead of Equation 3 we will now have the following:

$$V = \sum_i \frac{j_i H \alpha_i \tilde{S}_i}{\sigma_0 S_\mathrm{E}} \left(\exp\left(-\frac{z_i^\mathrm{l}}{H}\right) - \exp\left(-\frac{z_i^\mathrm{u}}{H}\right)\right)$$

with

$$\alpha_i = \begin{cases} kP_i/W_i, & \varepsilon_i \geq \varepsilon_0 \text{ and } T_i \geq T_0, \\ 0, & \text{otherwise} \end{cases}$$

and $j_i = c(T_i - T_0)$ provided that $\alpha_i > 0$, k and c being some constant coefficients. Then instead of Equation 4 we shall arrive at the following parameterization (as before, constant coefficients are omitted):

$$V \propto \sum_i \frac{\tilde{S}_i P_i}{W_i} (T_i - T_0) \left(\exp\left(-\frac{z_i^\mathrm{l}}{H}\right) - \exp\left(-\frac{z_i^\mathrm{u}}{H}\right)\right) \times \begin{cases} 1, & \varepsilon_i \geq \varepsilon_0 \text{ and } T_i \geq T_0, \\ 0, & \text{otherwise.} \end{cases} \tag{5}$$

In the parameterization given by Equation 5 we set $\varepsilon_0 = 0.5$ kJ/kg (which is even smaller than the lowest value considered before). Comparing Figure 3b with Figures 3d and 3f, we see that T_0 should be chosen somewhere between 22 and 26°C in order to set mid-latitude contributions to zero during the local winter; we set $T_0 = 25$°C since this value turns out to yield diurnal and seasonal variation cycles which are closest to their counterparts based on observations. The new simulated variations, resulting from the application of Equation 5 to the results of simulations with the WRF for 1980–2020, are shown in Figures 6e and 6f. Similarly to Figure 6d, Figure 6f also demonstrates the decomposition of the seasonal variation into contributions of different latitude ranges. The average contribution of the 9°S–9°N latitude range (indicated in the figure by shades of orange) is now about 58% of the total IP instead of 62% in the case of Figure 6d, and the peak-to-peak amplitude of this contribution has also become somewhat smaller (58% of the mean instead of 63%).

The diurnal variation of the IP obtained with Equation 5 still has generally the same shape as the diurnal PG cycle at Vostok and the classical Carnegie curve. Moreover, our modification of the parameterization substantially increased the peak-to-peak amplitude of the simulated diurnal variation (from 17% to 27%), thus making it more realistic (compare Figures 6a, 6c, and 6e), which appears to be impossible if one tries to express the IP in terms of convection alone (Ilin et al., 2020). At the same time the new seasonal behavior (Figure 6f) is much closer to the variation at Vostok (Figure 6b) than the patterns of variation based on the original parameterization given by Equation 4 (see Figure 6d and, more generally, Figures 5a–5h). In Figure 6d, based on Equation 4, the Northern Hemisphere summer is characterized by a pronounced local minimum in the IP, which generally contradicts the observations. On the other hand, the IP simulated with Equation 5, whose variation is shown in Figure 6f, attains the maximum in May; the values for June–August are only slightly lower, and we can say that the IP given by Equation 5 reaches highest values during the Northern Hemisphere summer, similarly to the Vostok variation and the variations inferred from air—Earth current measurements (cf. Scrase, 1933, Figure 4; Retalis, 1991, Figure 6; Adlerman & Williams, 1996, Figure 6).

Looking at Figures 6d and 6f, we note that our modification of the IP parameterization did not lead to significant changes in the seasonal behavior of contributions of different latitude ranges. The equatorial region still manifests a variation with two maxima which follow the equinoxes, whereas the contributions of higher latitudes are still larger during the local summer and smaller during the local winter. At the same time the resulting variation is completely different, having a maximum during the boreal summer instead of a minimum. This once again illustrates the subtlety of the seasonal effect in the GEC and highlights the difficulty of reproducing this effect in simulations.

It is also interesting to note that the peak-to-peak amplitude of the IP variation simulated using the new parameterization (13% of the mean) is much closer to the amplitude of the variation based on adjusted Vostok PG data (16%) than to its counterpart for unadjusted PG values (30%; compare Figures 2i, 2j, and 6f). Considering that the adjustment procedures which we employed are rather rough and empirical in their nature, we cannot be entirely certain of their accuracy; in this connection, our present observation implicitly suggests that the seasonal variation based on adjusted PG values is more representative of the real GEC. Also, if the actual seasonal variation of the GEC had the amplitude of 30%, it would probably be much easier to obtain such pattern in simulations.

One should not think that the parameterization given by Equation 5 will allow us to explain all the discrepancies between simulations and observations concerning the GEC variation on different timescales. Comparing Figures 6a and 6e, we already see that the diurnal maximum of the IP simulated with Equation 5 still occurs earlier than that of the Vostok PG (and the same is true for the diurnal minimum). A more detailed analysis shows that such discrepancies can be even more prominent if we consider the diurnal variation of the GEC during specific seasons of the year. Apart from that, our decision to make the source current density a function of the surface air temperature under an electrified cloud lacks any clear physical substantiation. Therefore, here we do not make any definitive conclusions and merely show the direction in which one can develop IP parameterizations for models of atmospheric dynamics. Our simulations just demonstrate that certain modifications of the parameterization aimed at enhancing the nonequatorial contribution to the GEC are actually able to produce a seasonal variation similar to that found in observations without disturbing the shape of the diurnal variation.

5. Conclusions

Although the results of simulations are even more ambiguous than the results of various measurements, which were considered in Part 1 of this study, we can still draw certain conclusions from our analysis. Let us summarize the main findings of this study.

1. From a theoretical perspective, the annual behavior of the GEC is determined by the seasonal dynamics of regional contributions to the IP, which, in its turn, reflects seasonal changes in the geographical distribution of convection. Therefore, the variation of contributions to the GEC from different latitude ranges is ultimately determined by local insolation cycles together with the distribution of land over the Earth's surface (since land is more responsive to changes in insolation than the ocean).
2. There is plenty of evidence indicating the existence of a stable annual variation pattern in the GEC intensity; however, this pattern is difficult to reliably determine from both observations and simulations. Taking the available results of measurements of atmospheric electrical parameters into consideration, it is likely that the actual GEC intensity is highest during the Northern Hemisphere summer and lowest during the Northern Hemisphere winter.
3. The magnitude of the variation is less clear; for example, the peak-to-peak amplitude of the seasonal variation based on the results of PG measurements at the Vostok station in Antarctica becomes more than two times smaller if one empirically adjusts the data for local meteorological and solar wind influences. At the same time a smaller amplitude appears to better agree with the results of simulations and is consistent with the difficulty of reproducing the effect in modeling.
4. Simulations indicate that the contribution to the GEC from the vicinity of the equator (say, the 9°S–9°N latitude range) has two maxima following the equinoxes, whereas the contribution of higher latitudes in each hemisphere has one maximum during the local summer (following the solstice). These patterns are very pronounced, and simulations reproduce them similarly regardless of the IP parameterization and the model of atmospheric dynamics employed. The simulated patterns allow a clear interpretation in terms of local insolation cycles at different latitudes.
5. When the three prominent regional patterns of variation are added up together, they offset each other, the two minima of the equatorial contribution being counterbalanced by the maxima of the nonequatorial ones. As a result, the variation of the total IP turns out to be much less pronounced than its constituent parts, and in simulations its shape can be different depending on the details of the model and the IP parameterization.
6. A combination of equatorial and nonequatorial seasonal patterns, which mirror local insolation cycles, is able to provide a qualitative physical explanation for the annual maximum in the GEC intensity during the Northern Hemisphere summer, with the dominance of this hemisphere related to it having more land mass. Moreover, one can also attribute a small local minimum in July amid the summer maximum, observed in the PG variation at the Vostok station, to the shape of the variation of the equatorial contribution to the IP, determined by the insolation cycle in the tropics.

7. Physical parameters which characterize convection do not provide a perfect measure of contributions to the IP, notably overestimating the role of equatorial latitudes; this often results in a poor representation in simulations of the seasonal variation of the total GEC intensity. By altering the IP parameterization through taking into account other variables (e.g., surface air temperature), one can increase nonequatorial contributions to the GEC and achieve a better agreement between simulations and observations. This indicates a direction in which GEC modeling can be further developed.

Data Availability Statement

PG data from Vostok for 2006–2020, source codes, and scripts used to analyze the results and plot images are available at https://zenodo.org/records/13898860 (Slyunyaev et al., 2025a). Adjustment of the Vostok data for meteorological and solar wind influences required weather data from Vostok (available, e.g., at https://rp5.ru/Weather_archive_at_Vostok_Station), the Weimer 2005 model (available at https://zenodo.org/records/2530324; see Weimer, 2005a, 2005b, 2019), and the hourly average OMNI data from the NASA (National Aeronautics and Space Administration) GSFC (Goddard Space Flight Center) Space Physics Data Facility (available at https://omniweb.gsfc.nasa.gov/ow.html; see King & Papitashvili, 2005; Papitashvili & King, 2020). The WRF-ARW model can be downloaded from https://www2.mmm.ucar.edu/wrf/users. Simulations with the WRF model used the ERA5 data (Hersbach et al., 2023), downloaded from the Copernicus Climate Change Service (C3S) Climate Data Store, so that their results contain modified C3S information 2021; neither the European Commission nor the European Centre for Medium-Range Weather Forecasts is responsible for any use that may be made of the Copernicus information or data it contains. Some variables were calculated using the wrf-python package (Ladwig, 2017).

Acknowledgments

NNS, FGS, NVI, and EAM acknowledge the state assignment of the Institute of Applied Physics of the Russian Academy of Sciences (NNS, NVI, and EAM: project no. FFUF-2023-0004; NNS, FGS, and NVI: project no. FFUF-2022-0008). The authors are grateful to the Australian Antarctic Division and to Gary Burns, the chief investigator of the project "Atmospheric electrical circuits, weather and climate research," for their contribution to the development of instruments and software for collecting the electric field data at the Vostok station. Continuous registration and collection of the electric field data at Vostok were carried out by the specialists of the Russian Antarctic Expedition within the framework of the project "Integrated oceanological, climatic, glaciological, and geophysical studies of Antarctica and the Southern Ocean."

References

Adlerman, E. J., & Williams, E. R. (1996). Seasonal variation of the global electrical circuit. *Journal of Geophysical Research*, *101*(D23), 29679–29688. https://doi.org/10.1029/96JD01547

Ault, J. P., & Mauchly, S. J. (1926). Atmospheric electric results obtained aboard the Carnegie, 1915–1921. In *Ocean magnetic and electric observations, 1915–1921* (pp. 195–286). Carnegie Institution of Washington. Retrieved from https://archive.org/details/oceanmagneticele00carn

Burns, G. B., Frank-Kamenetsky, A. V., Tinsley, B. A., French, W. J., Grigioni, P., Camporeale, G., & Bering, E. A. (2017). Atmospheric global circuit variations from Vostok and Concordia electric field measurements. *Journal of the Atmospheric Sciences*, *74*(3), 783–800. https://doi.org/10.1175/JAS-D-16-0159.1

Burns, G. B., Tinsley, B. A., Frank-Kamenetsky, A. V., Troshichev, O. A., French, W. J. R., & Klekociuk, A. R. (2012). Monthly diurnal global atmospheric circuit estimates derived from Vostok electric field measurements adjusted for local meteorological and solar wind influences. *Journal of the Atmospheric Sciences*, *69*(6), 2061–2082. https://doi.org/10.1175/JAS-D-11-0212.1

Emanuel, K. (2024). On the physics of high CAPE. *Journal of the Atmospheric Sciences*, *80*(11), 2669–2683. https://doi.org/10.1175/JAS-D-23-0060.1

Gertler, C. G., O'Gorman, P. A., & Pfahl, S. (2023). Moist available potential energy of the mean state of the atmosphere and the thermodynamic potential for warm conveyor belts and convection. *Weather and Climate Dynamics*, *4*(2), 361–379. https://doi.org/10.5194/wcd-4-361-2023

Halliday, E. C. (1933). Variations in the electric field in the atmosphere measured in Johannesburg, South Africa, during 1929 and 1930. *Terrestrial Magnetism and Atmospheric Electricity*, *38*(1), 37–53. https://doi.org/10.1029/TE038i001p00037

Harrison, R. G. (2003). Twentieth-century atmospheric electrical measurements at the observatories of Kew, Eskdalemuir and Lerwick. *Weather*, *58*(1), 11–19. https://doi.org/10.1256/wea.239.01

Harrison, R. G., & Ingram, W. J. (2005). Air–Earth current measurements at Kew, London, 1909–1979. *Atmospheric Research*, *76*(1–4), 49–64. https://doi.org/10.1016/j.atmosres.2004.11.022

Harrison, R. G., & Nicoll, K. A. (2008). Air-Earth current density measurements at Lerwick; implications for seasonality in the global electric circuit. *Atmospheric Research*, *89*(1–2), 181–193. https://doi.org/10.1016/j.atmosres.2008.01.008

Harrison, R. G., Nicoll, K. A., Joshi, M., & Hawkins, E. (2022). Empirical evidence for multidecadal scale global atmospheric electric circuit modulation by the El Niño-Southern Oscillation. *Environmental Research Letters*, *17*(12), 124048. https://doi.org/10.1088/1748-9326/aca68c

Hersbach, H., Bell, B., Berrisford, P., Biavati, G., Horányi, A., Muñoz Sabater, J., et al. (2023). ERA5 hourly data on pressure levels from 1940 to present [Dataset]. *Copernicus Climate Change Service (C3S) Climate Data Store (CDS)*. https://doi.org/10.24381/cds.bd0915c6

Hutchins, M. L., Holzworth, R. H., & Brundell, J. B. (2014). Diurnal variation of the global electric circuit from clustered thunderstorms. *Journal of Geophysical Research: Space Physics*, *119*(1), 620–629. https://doi.org/10.1002/2013JA019593

Ilin, N. V., Slyunyaev, N. N., & Mareev, E. A. (2020). Toward a realistic representation of global electric circuit generators in models of atmospheric dynamics. *Journal of Geophysical Research: Atmospheres*, *125*(6), e2019JD032130. https://doi.org/10.1029/2019JD032130

Jánský, J., Lucas, G. M., Kalb, C., Bayona, V., Peterson, M. J., Deierling, W., et al. (2017). Analysis of the diurnal variation of the global electric circuit obtained from different numerical models. *Journal of Geophysical Research: Atmospheres*, *122*(23), 12906–12917. https://doi.org/10.1002/2017JD026515

King, J. H., & Papitashvili, N. E. (2005). Solar wind spatial scales in and comparisons of hourly Wind and ACE plasma and magnetic field data. *Journal of Geophysical Research*, *110*(A2), A02104. https://doi.org/10.1029/2004JA010649

Kozlov, A. V., Slyunyaev, N. N., Ilin, N. V., Sarafanov, F. G., & Frank-Kamenetsky, A. V. (2023). The effect of the Madden–Julian Oscillation on the global electric circuit. *Atmospheric Research*, *284*, 106585. https://doi.org/10.1016/j.atmosres.2022.106585

Ladwig, W. (2017). wrf-python (version 1.3.2) [Software]. *UCAR/NCAR*. https://doi.org/10.5065/D6W094P1

Lavigne, T., Liu, C., Deierling, W., & Mach, D. (2017). Relationship between the global electric circuit and electrified cloud parameters at diurnal, seasonal, and interannual timescales. *Journal of Geophysical Research: Atmospheres*, *122*(16), 8525–8542. https://doi.org/10.1002/2016JD026442

Liu, C., Williams, E. R., Zipser, E. J., & Burns, G. (2010). Diurnal variations of global thunderstorms and electrified shower clouds and their contribution to the global electrical circuit. *Journal of the Atmospheric Sciences*, *67*(2), 309–323. https://doi.org/10.1175/2009JAS3248.1

Lucas, G. M., Baumgaertner, A. J. G., & Thayer, J. P. (2015). A global electric circuit model within a community climate model. *Journal of Geophysical Research: Atmospheres*, *120*(23), 12054–12066. https://doi.org/10.1002/2015JD023562

Ludlam, F. H. (1963). Severe local storms: A review. In *Severe local storms* (pp. 1–32). American Meteorological Society. (Meteorological Monographs, V. 5, No. 27). https://doi.org/10.1007/978-1-940033-56-3_1

Mach, D. M., Blakeslee, R. J., & Bateman, M. G. (2011). Global electric circuit implications of combined aircraft storm electric current measurements and satellite-based diurnal lightning statistics. *Journal of Geophysical Research*, *116*(D5), D05201. https://doi.org/10.1029/2010JD014462

Mareev, E. A., & Volodin, E. M. (2014). Variation of the global electric circuit and ionospheric potential in a general circulation model. *Geophysical Research Letters*, *41*(24), 9009–9016. https://doi.org/10.1002/2014GL062352

Markson, R. (1986). Tropical convection, ionospheric potentials and global circuit variation. *Nature*, *320*(6063), 588–594. https://doi.org/10.1038/320588a0

Markson, R. (2007). The global circuit intensity: Its measurement and variation over the last 50 years. *Bulletin of the American Meteorological Society*, *88*(2), 223–241. https://doi.org/10.1175/BAMS-88-2-223

Markson, R., Ruhnke, L. H., & Williams, E. R. (1999). Global scale comparison of simultaneous ionospheric potential measurements. *Atmospheric Research*, *51*(3–4), 315–321. https://doi.org/10.1016/S0169-8095(99)00016-2

Mauchly, S. J. (1921). Note on the diurnal variation of the atmospheric-electric potential-gradient. *Physical Review*, *18*(2), 161–162. https://doi.org/10.1103/PhysRev.18.85

Mauchly, S. J. (1923). On the diurnal variation of the potential gradient of atmospheric electricity. *Terrestrial Magnetism and Atmospheric Electricity*, *28*(3), 61–81. https://doi.org/10.1029/TE028i003p00061

Mezuman, K., Price, C., & Galanti, E. (2014). On the spatial and temporal distribution of global thunderstorm cells. *Environmental Research Letters*, *9*(12), 124023. https://doi.org/10.1088/1748-9326/9/12/124023

Mühleisen, R. (1971). New determination of the air-Earth current over the ocean and measurements of ionosphere potentials. *Pure and Applied Geophysics*, *84*(1), 112–115. https://doi.org/10.1007/BF00875459

Mühleisen, R. (1977). The global circuit and its parameters. In H. Dolezalek, & R. Reiter (Eds.), *Electrical processes in atmospheres* (pp. 467–476). Steinkopff. https://doi.org/10.1007/978-3-642-85294-7_73

Papitashvili, N. E., & King, J. H. (2020). OMNI hourly data [Dataset]. *NASA Space Physics Data Facility*. https://doi.org/10.48322/1shr-ht18

Peterson, M. (2024). The thunderstorms with the greatest lightning densities on Earth. *Earth and Space Science*, *11*(1), e2023EA003304. https://doi.org/10.1029/2023EA003304

Powers, J. G., Klemp, J. B., Skamarock, W. C., Davis, C. A., Dudhia, J., Gill, D. O., et al. (2017). The Weather Research and Forecasting model: Overview, system efforts, and future directions. *Bulletin of the American Meteorological Society*, *98*(8), 1717–1737. https://doi.org/10.1175/BAMS-D-15-00308.1

Retalis, D. A. (1991). Study of the air-Earth electrical current density in Athens. *Pure and Applied Geophysics*, *136*(2–3), 217–233. https://doi.org/10.1007/BF00876374

Rycroft, M. J., Harrison, R. G., Nicoll, K. A., & Mareev, E. A. (2008). An overview of Earth's global electric circuit and atmospheric conductivity. *Space Science Reviews*, *137*(1–4), 83–105. https://doi.org/10.1007/s11214-008-9368-6

Scrase, F. J. (1933). *The air-Earth current at Kew Observatory*. H. M. Stationery Office. Retrieved from https://digital.nmla.metoffice.gov.uk/IO_78a2c258-0c8c-4eed-9654-855eec72bc81

Simpson, C. G. (1906). III. Atmospheric electricity in high latitudes. *Philosophical Transactions of the Royal Society of London A*, *205*, 61–97. https://doi.org/10.1098/rsta.1906.0003

Skamarock, W. C., Klemp, J. B., Dudhia, J., Gill, D. O., Liu, Z., Berner, J., et al. (2019). *A description of the advanced research WRF version 4*. NCAR Technical Note NCAR/TN-556+STR. https://doi.org/10.5065/1dfh-6p97

Slyunyaev, N., Sarafanov, F., Ilin, N., Mareev, E., Volodin, E., Frank-Kamenetsky, A., & Williams, E. (2025a). Data and code for articles on the seasonal variation of the DC global electric circuit [Dataset]. *Zenodo*. https://doi.org/10.5281/zenodo.13898860

Slyunyaev, N. N., Frank-Kamenetsky, A. V., Ilin, N. V., Sarafanov, F. G., Shatalina, M. V., Mareev, E. A., & Price, C. G. (2021). Electric field measurements in the Antarctic reveal patterns related to the El Niño—Southern Oscillation. *Geophysical Research Letters*, *48*(21), e2021GL095389. https://doi.org/10.1029/2021GL095389

Slyunyaev, N. N., Ilin, N. V., Mareev, E. A., & Price, C. G. (2021). The global electric circuit land–ocean response to the El Niño—Southern Oscillation. *Atmospheric Research*, *260*, 105626. https://doi.org/10.1016/j.atmosres.2021.105626

Slyunyaev, N. N., Mareev, E. A., Kalinin, A. V., & Zhidkov, A. A. (2014). Influence of large-scale conductivity inhomogeneities in the atmosphere on the global electric circuit. *Journal of the Atmospheric Sciences*, *71*(11), 4382–4396. https://doi.org/10.1175/JAS-D-14-0001.1

Slyunyaev, N. N., Sarafanov, F. G., Ilin, N. V., Mareev, E. A., Volodin, E. M., Frank-Kamenetsky, A. V., & Williams, E. R. (2025b). The seasonal variation of the direct current global electric circuit: 1. A new analysis based on long-term measurements in Antarctica. *Journal of Geophysical Research: Atmospheres*, *130*(6), e2024JD042633. https://doi.org/10.1029/2024jd042633

Sverdrup, H. U. (1926). Scientific work of the Maud Expedition, 1922–1925. *The Scientific Monthly*, *22*(5), 400–410. Retrieved from https://www.jstor.org/stable/7648

Tacza, J., Nicoll, K. A., & Macotela, E. (2022). Periodicities in fair weather potential gradient data from multiple stations at different latitudes. *Atmospheric Research*, *276*, 106250. https://doi.org/10.1016/j.atmosres.2022.106250

Thomson, W. (1860). Atmospheric electricity. In J. P. Nichol (Ed.), *A cyclopedia of the physical sciences* (2nd ed., pp. 267–274). Richard Griffin. Retrieved from https://archive.org/details/b21496079

Thomson, W. (1884). Atmospheric electricity. In *Reprint of papers on electrostatics and magnetism* (2nd ed., pp. 192–239). Macmillan. Retrieved from https://archive.org/details/reprintofpaperso00kelvrich

Tinsley, B. A., & Zhou, L. (2006). Initial results of a global circuit model with variable stratospheric and tropospheric aerosols. *Journal of Geophysical Research*, *111*(D16), D16205. https://doi.org/10.1029/2005JD006988

Torreson, O. W., Parkinson, W. C., Gish, O. H., & Wait, G. R. (1946). *Ocean atmospheric-electric results (Scientific results of Cruise VII of the Carnegie during 1928–1929 under command of captain J. P. Ault, Oceanography—III)*. Carnegie Institution of Washington. Retrieved from https://archive.org/details/oceanatmospheric00carn

Volodin, E. M. (2023). Simulation of present-day climate with the INMCM60 model. *Izvestiya—Atmospheric and Oceanic Physics*, *59*(1), 16–22. https://doi.org/10.1134/S0001433823010139

Weimer, D. (2019). Weimer 2005 ionospheric electric potential model for IDL [Software]. *Zenodo*. https://doi.org/10.5281/zenodo.2530324

Weimer, D. R. (2005a). Improved ionospheric electrodynamic models and application to calculating Joule heating rates. *Journal of Geophysical Research*, *110*(A5), A05306. https://doi.org/10.1029/2004JA010884

Weimer, D. R. (2005b). Predicting surface geomagnetic variations using ionospheric electrodynamic models. *Journal of Geophysical Research*, *110*(A12), A12307. https://doi.org/10.1029/2005JA011270

Whipple, F. J. W. (1929). On the association of the diurnal variation of electric potential gradient in fine weather with the distribution of thunderstorms over the globe. *Quarterly Journal of the Royal Meteorological Society*, *55*(229), 1–18. https://doi.org/10.1002/qj.49705522902

Whipple, F. J. W., & Scrase, F. J. (1936). *Point discharge in the electric field of the Earth: An analysis of continuous records obtained at Kew Observatory*. H. M. Stationery Office. Retrieved from https://digital.nmla.metoffice.gov.uk/IO_efb7fd62-a542-4266-aac6-cbdeae3311b6

Williams, E., & Mareev, E. (2014). Recent progress on the global electrical circuit. *Atmospheric Research*, *135–136*, 208–227. https://doi.org/10.1016/j.atmosres.2013.05.015

Williams, E. R. (1994). Global circuit response to seasonal variations in global surface air temperature. *Monthly Weather Review*, *122*(8), 1917–1929. https://doi.org/10.1175/1520-0493(1994)122<1917:GCRTSV>2.0.CO;2

Williams, E. R. (2009). The global electrical circuit: A review. *Atmospheric Research*, *91*(2–4), 140–152. https://doi.org/10.1016/j.atmosres.2008.05.018

Wilson, C. T. R. (1921). Investigations on lightning discharges and on the electric field of thunderstorms. *Philosophical Transactions of the Royal Society of London A*, *221*, 73–115. https://doi.org/10.1098/rsta.1921.0003

References From the Supporting Information

Betts, A. K. (1986). A new convective adjustment scheme. Part I: Observational and theoretical basis. *Quarterly Journal of the Royal Meteorological Society*, *112*(473), 677–691. https://doi.org/10.1002/qj.49711247307

Betts, A. K., & Miller, M. J. (1986). A new convective adjustment scheme. Part II: Single column tests using GATE wave, BOMEX, ATEX and arctic air-mass data sets. *Quarterly Journal of the Royal Meteorological Society*, *112*(473), 693–709. https://doi.org/10.1002/qj.49711247308

Janjić, Z. I. (1994). The step-mountain eta coordinate model: Further developments of the convection, viscous sublayer, and turbulence closure schemes. *Monthly Weather Review*, *122*(5), 927–945. https://doi.org/10.1175/1520-0493(1994)122<0927:TSMECM>2.0.CO;2

Janjić, Z. I. (2000). Comments on "Development and evaluation of a convection scheme for use in climate models". *Journal of the Atmospheric Sciences*, *57*(21), 3686. https://doi.org/10.1175/1520-0469(2000)057<3686:CODAEO>2.0.CO;2

Lin, Y., Farley, R. D., & Orville, H. D. (1983). Bulk parameterization of the snow field in a cloud model. *Journal of Climate and Applied Meteorology*, *22*(6), 1065–1092. https://doi.org/10.1175/1520-0450(1983)022<1065:BPOTSF>2.0.CO;2